Astronomy & Astrophysics manuscript no. AA-2011-16459
July 8, 2011

Planck early results VIII: The all-sky early Sunyaev-Zeldovich cluster sample

Planck Collaboration: P. A. R. Ade[77], N. Aghanim[50], M. Arnaud[62], M. Ashdown[60,4], J. Aumont[50], C. Baccigalupi[75], A. Balbi[31], A. J. Banday[85,7,68], R. B. Barreiro[57], M. Bartelmann[83,68], J. G. Bartlett[3,58], E. Battaner[88], R. Battye[59], K. Benabed[51], A. Benoît[49], J.-P. Bernard[85,7], M. Bersanelli[28,44], R. Bhatia[5], J. J. Bock[58,8], A. Bonaldi[40], J. R. Bond[6], J. Borrill[66,79], F. R. Bouchet[51], M. L. Brown[4,60], M. Bucher[3], C. Burigana[43], P. Cabella[31], C. M. Cantalupo[66], J.-F. Cardoso[63,3,51], P. Carvalho[4], A. Catalano[3,61], L. Cayón[21], A. Challinor[54,60,11], A. Chamballu[47], R.-R. Chary[48], L.-Y Chiang[53], C. Chiang[20], G. Chon[69,4], P. R. Christensen[72,32], E. Churazov[68,78], D. L. Clements[47], S. Colafrancesco[41], S. Colombi[51], F. Couchot[65], A. Coulais[61], B. P. Crill[58,73], F. Cuttaia[43], A. Da Silva[10], H. Dahle[55,9], L. Danese[75], R. J. Davis[59], P. de Bernardis[27], G. de Gasperis[31], A. de Rosa[43], G. de Zotti[40,75], J. Delabrouille[3], J.-M. Delouis[51], F.-X. Désert[46], C. Dickinson[59], J. M. Diego[57], K. Dolag[68], H. Dole[50], S. Donzelli[44,55], O. Doré[58,8], U. Dörl[68], M. Douspis[50]⋆, X. Dupac[36], G. Efstathiou[54], P. Eisenhardt[58], T. A. Enßlin[68], F. Feroz[4], F. Finelli[43], I. Flores-Cacho[56,33], O. Forni[85,7], P. Fosalba[52], M. Frailis[42], E. Franceschi[43], S. Fromenteau[3,50], S. Galeotta[42], K. Ganga[3,48], R. T. Génova-Santos[56,33], M. Giard[85,7], G. Giardino[37], Y. Giraud-Héraud[3], J. González-Nuevo[75], R. González-Riestra[35], K. M. Górski[58,90], K. J. B. Grainge[4,60], S. Gratton[60,54], A. Gregorio[29], A. Gruppuso[43], D. Harrison[54,60], P. Heinämäki[82], S. Henrot-Versillé[65], C. Hernández-Monteagudo[68], D. Herranz[57], S. R. Hildebrandt[8,64,56], E. Hivon[51], M. Hobson[4], W. A. Holmes[58], W. Hovest[68], R. J. Hoyland[56], K. M. Huffenberger[89], G. Hurier[64], N. Hurley-Walker[4], A. H. Jaffe[47], W. C. Jones[20], M. Juvela[19], E. Keihänen[19], R. Keskitalo[58,19], T. S. Kisner[66], R. Kneissl[34,5], L. Knox[23], H. Kurki-Suonio[19,39], G. Lagache[50], J.-M. Lamarre[61], A. Lasenby[4,60], R. J. Laureijs[37], C. R. Lawrence[58], M. Le Jeune[3], S. Leach[75], R. Leonardi[36,37,24], C. Li[67,68], A. Liddle[18], P. B. Lilje[55,9], M. Linden-Vørnle[13], M. López-Caniego[57], P. M. Lubin[24], J. F. Macías-Pérez[64], C. J. MacTavish[60], B. Maffei[59], D. Maino[28,44], N. Mandolesi[43], R. Mann[76], M. Maris[42], F. Marleau[15], E. Martínez-González[57], S. Masi[27], S. Matarrese[26], F. Matthai[68], P. Mazzotta[31], S. Mei[84,38,8], P. R. Meinhold[24], A. Melchiorri[27], J.-B. Melin[12], L. Mendes[36], A. Mennella[28,42], S. Mitra[58], M.-A. Miville-Deschênes[50,6], A. Moneti[51], L. Montier[85,7], G. Morgante[43], D. Mortlock[47], D. Munshi[77,54], A. Murphy[71], P. Naselsky[72,32], F. Nati[27], P. Natoli[30,2,43], C. B. Netterfield[15], H. U. Nørgaard-Nielsen[13], F. Noviello[50], D. Novikov[47], I. Novikov[72], M. Olamaie[4], S. Osborne[80], F. Pajot[50], F. Pasian[42], G. Patanchon[3], T. J. Pearson[8,48], O. Perdereau[65], L. Perotto[64], F. Perrotta[75], F. Piacentini[27], M. Piat[3], E. Pierpaoli[17], R. Piffaretti[62,12], S. Plaszczynski[65], E. Pointecouteau[85,7], G. Polenta[2,41], N. Ponthieu[50], T. Poutanen[39,19,1], G. W. Pratt[62], G. Prézeau[8,58], S. Prunet[51], J.-L. Puget[50], J. P. Rachen[68], W. T. Reach[86], R. Rebolo[56,33], M. Reinecke[68], C. Renault[64], S. Ricciardi[43], T. Riller[68], I. Ristorcelli[85,7], G. Rocha[58,8], C. Rosset[3], J. A. Rubiño-Martín[56,33], B. Rusholme[48], E. Saar[81], M. Sandri[43], D. Santos[64], R. D. E. Saunders[4,60], G. Savini[74], B. M. Schaefer[83], D. Scott[16], M. D. Seiffert[58,8], P. Shellard[11], G. F. Smoot[22,66,3], A. Stanford[23], J.-L. Starck[62,12], F. Stivoli[45], V. Stolyarov[4], R. Stompor[3], R. Sudiwala[77], R. Sunyaev[68,78], D. Sutton[54,60], J.-F. Sygnet[51], N. Taburet[50], J. A. Tauber[37], L. Terenzi[43], L. Toffolatti[14], M. Tomasi[28,44], J.-P. Torre[50], M. Tristram[65], J. Tuovinen[70], L. Valenziano[43], L. Vibert[50], P. Vielva[57], F. Villa[43], N. Vittorio[31], L. A. Wade[58], B. D. Wandelt[51,25], J. Weller[87], S. D. M. White[68], M. White[22], D. Yvon[12], A. Zacchei[42], and A. Zonca[24]

(Affiliations can be found after the references)

Preprint online version: July 8, 2011

ABSTRACT

We present the first all-sky sample of galaxy clusters detected blindly by the *Planck* satellite through the Sunyaev-Zeldovich (SZ) effect from its six highest frequencies. This early SZ (ESZ) sample is comprised of 189 candidates, which have a high signal-to-noise ratio ranging from 6 to 29. Its high reliability (purity above 95%) is further ensured by an extensive validation process based on *Planck* internal quality assessments and by external cross-identification and follow-up observations. *Planck* provides the first measured SZ signal for about 80% of the 169 previously-known ESZ clusters. *Planck* furthermore releases 30 new cluster candidates, amongst which 20 meet the ESZ signal-to-noise selection criterion. At the submission date, twelve of the 20 ESZ candidates were confirmed as new clusters, with eleven confirmed using XMM-Newton snapshot observations, most of them with disturbed morphologies and low luminosities. The ESZ clusters are mostly at moderate redshifts (86% with z below 0.3) and span more than a decade in mass, up to the rarest and most massive clusters with masses above $1 \times 10^{15}\ M_{\odot}$.

Key words. Galaxy Clusters – Large-Scale Structure – Planck

1. Introduction

Galaxy clusters provide valuable information on cosmology, from the nature of dark energy to the physics that drives galaxy and structure formation. The main baryonic component in these dark matter dominated objects is a hot, ionised intra-cluster medium (ICM). The ICM can be studied both in the X-ray and through the Sunyaev-Zeldovich effect (SZ) (Sunyaev & Zeldovich 1972; Sunyaev & Zeldovich 1980), a fairly new and highly promising technique that has made tremendous progress in recent years since its first observations (Birkinshaw & Gull 1978); see also Rephaeli (1995); Birkinshaw (1999); Carlstrom et al. (2002).

The SZ effect is undoubtedly the best known and most studied secondary contribution, due to cosmic structure, that is imprinted on the cosmic microwave background after decoupling [for a review of secondary anisotropies see Aghanim et al. (2008)]. It is caused by the inverse Compton interaction between the cosmic microwave background (CMB) photons and the free

⋆ Corresponding author: M. Douspis, marian.douspis@ias.u-psud.fr

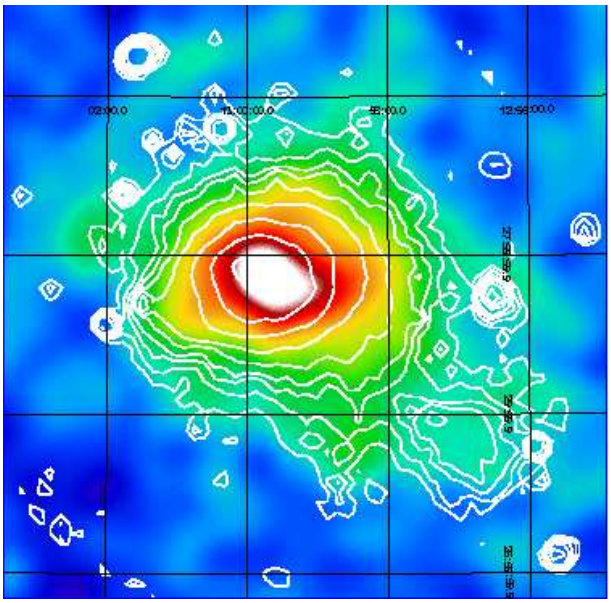

Fig. 1. *Planck* *y*-map of Coma on a $\sim 3^\circ \times 3^\circ$ patch with the *ROSAT-PSPC* iso-luminosity contours overlaid.

electrons of the hot ICM. It can be broadly subdivided into the thermal SZ (TSZ) effect, where the photons are scattered by the random motion of thermal electrons, and the kinetic SZ (KSZ) effect caused by the bulk motion of the electrons. In the former case, the scattered CMB photons have a unique spectral dependence, whereas the final spectrum remains Planckian in the case of the KSZ effect.

The SZ effect offers a number of advantages for cluster studies. First, the Compton *y* parameter, which measures the integral of the gas pressure along the line of sight and sets the amplitude of the SZ signal, does not suffer from cosmological surface-brightness dimming. This implies that the SZ effect is an efficient method for finding high-redshift clusters. Second, the total SZ signal *Y*, integrated over the cluster's angular extent, directly measures the total thermal energy of the gas and as such is expected to correlate closely (i.e., with a tight scatter in the scaling relation) with total cluster mass. This fact is borne out both by numerical simulations (Borgani 2006; da Silva et al. 2001; Motl et al. 2005; Pfrommer et al. 2007) and indirectly from X-ray observations (Nagai et al. 2007; Arnaud et al. 2007; Vikhlinin et al. 2009) using Y_X, the product of the gas mass and mean temperature giving an X-ray analogue of the integrated SZ Compton parameter first introduced by Kravtsov et al. (2006). This contrasts with the X-ray luminosity which, at a given mass, is very sensitive to the cluster's thermodynamical state, for instance due to a recent merger event or in the presence of a strong cooling core. Hence SZ surveys are expected to provide clean cluster samples over a wide range of redshifts, in the sense of being close to an unbiased mass-limited selection. These are key properties for statistical studies with clusters, either to constrain cosmological models (e.g., from the evolution of the mass function) or to probe the physics of structure formation (e.g., from cluster scaling and structural properties).

For these reasons, alongside the efforts developed to measure CMB anisotropies many pioneering instruments were used or developed to observe the SZ effect and use it as new observational probe of cluster physics, large-scale structure, and the cosmological model. The first observations of the SZ effect, targeted at specific X-ray selected clusters, were performed using interferometric or single-dish experiments mostly observing in the Rayleigh–Jeans part of the spectrum: the Ryle Telescope at 15 GHz (Jones et al. 1993), the OVRO 5 meter telescope at 32 GHz (Birkinshaw & Hughes 1994), the SuZIE array at 140 GHz (Holzapfel et al. 1997), BOLOCAM at 143 and 265 GHz (Glenn et al. 1998), the Diabolo array on IRAM 30 meter telescope at 140 GHz (Pointecouteau et al. 1999), MITO at 143, 214, 272, and 353 GHz (De Petris et al. 1999), the Nobeyama 45 metre telescope at 21 GHZ, 43 GHz and 150 GHz (Komatsu et al. 1999), the BIMA array at 30 GHz (Dawson et al. 2001), ACBAR at 150 and 220 GHz (Gómez et al. 2003), CBI working between 25 and 36 GHz (Udomprasert et al. 2004), VSA at 30 GHz (Lancaster et al. 2005), the Atacama Pathfinder Experiment (APEX) SZ Camera at 150 GHz (Dobbs et al. 2006), the SZ Array at 30 GHz (Muchovej et al. 2007), AMI at 15 GHz (Zwart et al. 2008), and AMIBA at 90GHz (Wu et al. 2008); see Birkinshaw & Lancaster (2005) for a review of observational techniques. Measurements of the SZ effect were further made or attempted in the Wien part of the spectrum with PRONAOS (Lamarre et al. 1998), SCUBA (Zemcov et al. 2007), and more recently with the Herschel Space Observatory (Zemcov et al. 2010).

These experiments have not only allowed us to accumulate SZ measurements for about a hundred clusters, but have also laid the groundwork for SZ-based studies of clusters and of cosmology. In combination with other observations, especially in X-rays, they were used to measure cosmological parameters such as the Hubble constant, and to probe the distance-duality relation between the angular-diameter and luminosity distances, bulk flows, and the cluster gas mass fraction [e.g., Silk & White (1978); Kobayashi et al. (1996); Grego et al. (2001); Reese et al. (2002); Uzan et al. (2004); Ameglio et al. (2006); Bonamente et al. (2006); Kashlinsky et al. (2008)]. The SZ effect has also been used to characterise the clusters themselves, as it can potentially measure their radial peculiar velocities (Benson et al. 2003). The relativistic corrections to the SZ effect (e.g., Itoh et al. (1998)) can be used to measure the gas temperature directly for massive clusters (Pointecouteau et al. 1998). The spectral signature of the SZ effect can in principle even probe the electron gas distribution and constrain any non-thermal electron population in the intracluster medium (Colafrancesco et al. 2003; Shimon & Rephaeli 2004). The SZ effect can also be used as a tracer of the WHIM diffuse gas (Génova-Santos et al. 2005; Battistelli et al. 2006). Moreover multi-frequency SZ measurements might provide a novel way of constraining the CMB temperature and its evolution with redshift (Battistelli et al. 2002; Horellou et al. 2005; Luzzi et al. 2009).

Deep surveys covering hundreds of square degrees and capable of detecting many tens to hundreds of clusters, performed by the South Pole Telescope (SPT) (Carlstrom et al. 2009) and the Atacama Cosmology Telescope (ACT) (Marriage et al. 2010), are accumulating, and already delivering, data. One of their goals is to use SZ cluster counts and the SZ angular correlation function as cosmological tools (Haiman et al. 2001; Weller et al. 2002; Levine et al. 2002; Majumdar & Mohr 2004; Douspis et al. 2006). Such surveys are particularly powerful for detecting distant clusters, as was recently proven by results from Vanderlinde et al. (2010).

In this context ESA's *Planck*[1] mission, launched on 14 May 2009, carries a scientific payload consisting of an array of 74 detectors sensitive to a range of frequencies between roughly 25 and 1000 GHz, which scan the sky simultaneously and continuously with an angular resolution varying between about 30 arcmin (FWHM) at the lowest frequencies and about four arcmin at the highest. The array is arranged into two instruments. The detectors of the Low Frequency Instrument (LFI) are pseudo-correlation radiometers covering three bands centred at 30, 44, and 70 GHz. The detectors of the High Frequency Instrument (Lamarre et al. 2010; Planck HFI Core Team 2011a, HFI;) are bolometers covering six bands centred at 100, 143, 217, 353, 545, and 857 GHz with bolometers cooled to 0.1 K. The design of *Planck* allows it to image the whole sky approximately twice per year, with an unprecedented combination of sensitivity, angular resolution, and frequency coverage. The *Planck* satellite, its payload, and its performance as predicted at the time of launch are described in 13 articles included in a special issue (Volume 520) of Astronomy & Astrophysics. The main objective of *Planck* is to measure the spatial anisotropies of the temperature of the Cosmic Microwave Background (CMB) with an accuracy set by fundamental astrophysical limits. Its level of performance will enable *Planck* to extract essentially all the information in the CMB temperature anisotropies. *Planck* will also measure to high accuracy the polarisation of the CMB anisotropies, which not only encodes a wealth of cosmological information but also provides a unique probe of the thermal history of the Universe during the time when the first stars and galaxies formed. In addition, the *Planck* sky surveys will produce a wealth of information on the dust and gas in our own galaxy and on the properties of extragalactic sources.

Planck was specifically designed from the beginning to measure the SZ effect (Aghanim et al. 1997) and provide us with an all-sky SZ cluster catalogue. The first galaxy cluster searched for in the HFI data, Abell 2163 (Fig. 5 and 6), was indeed found from 100 GHz to 353 GHz shortly after the First Light Survey (FLS) was performed and observations in routine mode by *Planck* started. Three other known clusters falling in the FLS region were seen across the positive and negative parts of the SZ spectrum. The scanning strategy soon allowed us to map extended clusters such as Coma on wide patches of the sky (Fig. 1). SZ detection techniques were then applied to the data and the first blind detections were performed.

The *Planck* all-sky SZ cluster catalogue, with clusters out to redshifts $z \sim 1$, that will be delivered to the community at the end of the mission will be the first all-sky cluster survey since the ROSAT All-Sky Survey (RASS), which was at much lower depth (the median redshift of the NORAS/REFLEX cluster catalogue is $z \simeq 0.1$). Thanks to its all-sky nature, *Planck* will detect the rarest clusters, i.e., the most massive clusters in the exponential tail of the mass function which are the best clusters for cosmological studies. The *Planck* Early SZ (ESZ) sample is delivered alongside the Early Release Compact Source Catalogue (ERCSC) (Planck Collaboration 2011a), the nine-band source catalogue, and the Early Cold Core (ECC) catalogue (Planck Collaboration 2011f) at *http://www.rssd.esa.int/Planck* (Planck Collaboration 2011g). The ESZ is a high-reliability sample of 189 SZ clusters or candidates detected over the whole sky from the first ten months of the *Planck* survey of the sky.

The present article details the process by which *Planck* ESZ sample was constructed and validated. The *Planck* data and the specific SZ extraction methods used to detect the SZ candidates are presented in Sections 2 and 3. *Planck*'s measurements provide an estimate of the integrated Compton parameter, Y, of detected SZ cluster "candidates". A subsequent validation process is needed to identify which among the candidates are previously known clusters, and an additional follow-up programme is required to scientifically exploit *Planck* cluster data. This includes cluster confirmation (catalogue validation) and the measurement of relevant physical parameters. These different steps of the ESZ construction and validation are presented in Section 4 and the subsequent results are given in Section 5. Finally, Sections 6, 7, and 8 present the general properties of the ESZ cluster sample. *Planck* early results on clusters of galaxies are presented here and in a set of accompanying articles (Planck Collaboration 2011b,c,d,e).

Throughout the article, and in all the above cited *Planck* SZ early result papers, the adopted cosmological model is a ΛCDM cosmology with Hubble constant, $H_0 = 70\ \mathrm{km\,s^{-1}\,Mpc^{-1}}$, matter density parameter $\Omega_\mathrm{m} = 0.3$ and dark energy density parameter $\Omega_\Lambda = 0.7$. The quantity $E(z)$ is the ratio of the Hubble constant at redshift z to its present value, H_0 , i.e., $E^2(z) = \Omega_\mathrm{m}(1+z)^3 + \Omega_\Lambda$.

2. *Planck* data description

The ESZ sample was constructed out of the *Planck* channel maps of the HFI instrument, as described in detail in Planck HFI Core Team (2011b). These maps correspond to the observations of the temperature in the first ten months of the survey by *Planck*, which give complete sky coverage. Raw data were first processed to produce cleaned time-lines (time-ordered information, TOI) and associated flags correcting for different systematic effects. This includes a low-pass filter, glitch treatment, conversion to units of absorbed power, and a decorrelation of thermal stage fluctuations. For cluster detection, and more generally for source detection, one data flag of special importance is associated with Solar System Objects (SSO). These objects were identified in TOI data using the publicly-available Horizon ephemeris, and the SSO flag was created to ensure that they are not projected onto the sky, in order to avoid possible false detections, ringing, etc.

Focal-plane reconstruction and beam-shape estimates were obtained using observations of Mars. Beams are described by an elliptical Gaussian parameterisation leading to FWHM θ_S given in Planck HFI Core Team (2011b). The attitude of the satellite as a function of time is provided by the two star trackers installed on the *Planck* spacecraft. The pointing for each bolometer was computed by combining the attitude with the location of the bolometer in the focal plane reconstructed from Mars observations.

From the cleaned TOI and the pointing, channel maps have been made by co-adding bolometers at a given frequency. The path from TOI to maps in the HFI data processing is schematically divided into three steps: ring-making, destriping, and map-making. The first step averages circles within a pointing period to make rings with higher signal-to-noise (S/N) ratio, taking advantage of the redundancy of observations provided by the *Planck* scanning strategy. The low amplitude $1/f$ component is accounted for in the second step using a destriping technique. Finally, cleaned maps are produced using a simple co-addition

[1] *Planck* (http://www.rssd.esa.int/Planck) is a project of the European Space Agency (ESA) with instruments provided by two scientific consortia funded by ESA member states (in particular the lead countries France and Italy), with contributions from NASA (USA) and telescope reflectors provided by a collaboration between ESA and a scientific consortium led and funded by Denmark.

of the Healpix-based rings[2]. SSO flag channel maps, used in the internal validation of the ESZ sample, were also made following the same procedure.

The noise in the channel maps is essentially white with a standard deviation of $1.6, 0.9, 1.4, 5.0, 70, 1180\,\mu$K degree[3] from low to high frequencies (Planck HFI Core Team 2011b). Photometric calibration is performed for the lower frequency channels at the ring level using the CMB dipole (from WMAP (Hinshaw et al. 2009)), and at the map level using FIRAS data (Fixsen et al. 1994) for the higher frequency channels at 545 and 857 GHz. The absolute gain calibration of HFI *Planck* maps is known to better than 2% (Planck HFI Core Team 2011b).

3. Detection and Cluster extraction

In order to generate a cluster candidate list, a suitable extraction algorithm must be run on the maps. SZ clusters can be considered as compact sources with respect to the *Planck* beam, but they are definitely not point sources. Their extension thus merits a special adapted processing. For this reason, several extraction methods were developed within the *Planck* collaboration, and those were tested and compared using the *Planck* Sky Model Simulation (PSM[4]). The details of the comparison of the cluster extraction algorithms, called the "SZ challenge", can be found in Melin et al. (in prep.).

Methods fall into two classes: "direct" methods use individual channel maps to extract the clusters, while "indirect" methods use sky y-maps obtained via component separation algorithms. The methods used in this article are direct methods, with the reference method chosen on the basis of the SZ challenge. The direct detection algorithms used to construct and validate the ESZ sample incorporate prior assumptions on the cluster signal, specifically its spectral and spatial [i.e., the shape of the Intra-Cluster Medium (ICM) pressure profile] characteristics (see Sect. 3.1). This enhances the cluster contrast over a set of observations containing contaminating signals.

Most of the methods developed prior to the launch were applied to the *Planck* data, but only direct methods were favoured for implementation in the pipeline infrastructure. The following three were used to construct and validate the ESZ sample:

- A matched multi-frequency filter (MMF) algorithm, referred to henceforth as MMF3, was the reference method used for the blind detection of SZ candidates, and the construction of the ESZ list.
- Two other methods (Sections 3.3.2 and 3.3.1) were used to confirm the blind detections of the ESZ candidates.

In addition, a slightly different version of MMF3 was run as part of ESZ validation, in order to re-extract the Compton Y parameter of the SZ clusters incorporating fixed cluster sizes and positions taken from X-ray observations (see Sect. 6.2).

3.1. Baseline cluster model

The ICM pressure profile has historically been described by an isothermal β-model (Cavaliere & Fusco-Femiano 1978; Grego et al. 2001; Reese et al. 2002, e.g.,). However, recent X-ray observations have shown that a β-model is a poor description of the gas distribution in clusters, leading several authors to propose more realistic analytical functions based on a Generalised Navarro-Frenk-and-White (GNFW) profile (Nagai et al. 2007; Arnaud et al. 2010).

The baseline pressure profile used in the present work is the standard "universal" pressure profile derived by Arnaud et al. (2010). It is constructed by combining the observed X-ray pressure profile within R_{500}, from 31 galaxy clusters of the REXCESS sample (Böhringer et al. 2007), with data from state-of-the-art numerical simulations (Borgani et al. 2004; Nagai et al. 2007; Piffaretti & Valdarnini 2008) out to $5\,R_{500}$. In the following, R_{500} is the cluster size defined as the radius where the mean enclosed density is 500 times the critical density. It relates to the characteristic cluster scale R_s through the NFW concentration parameter c_{500} ($R_s = R_{500}/c_{500}$).

The pressure profile model used in the present article is equivalent to the standard self-similar case described in Appendix B of Arnaud et al. (2010).[5] It is equivalent to a shape function characterised by two free parameters, a central value and a characteristic scale θ_s.

The SZ effect from the hot ICM is due to the first-order correction for energy transfer in Thomson scattering. There is a spectral distortion, energy being transferred from photons in the Rayleigh–Jeans tail of the cosmic blackbody radiation to the Wien tail. In the non-relativistic limit the frequency dependence of the distortion is universal (the same for all clusters), characterised by a distinct frequency, $\nu \sim 220$ GHz, where the TSZ effect vanishes. Below this frequency there is a decrement of the CMB intensity, giving an apparent *decrease* in the sky brightness, and above lies an enhancement.

The magnitude of the SZ effect, known as the Compton parameter y, depends only on the cluster's characteristics, electronic temperature T_e and density n_e, as

$$y = \frac{k\sigma_T}{m_e c^2} \int^l T_e(l) n_e(l)\, \mathrm{d}l$$

where k is the Boltzmann constant, σ_T the Thomson cross section, $m_e c^2$ the electron rest mass and l is the distance along the line of sight. The total SZ signal is characterised by the integrated Compton parameter denoted $Y = \int y\, \mathrm{d}\Omega$, where Ω is solid angle. It can be written as $D_A^2 Y = (\sigma_T/m_e c^2) \int PdV$, where D_A is the angular-diameter distance to the system and $P = n_e k T_e$ the electron pressure. In the following, the integral performed over the sphere of radius R_{500} ($5R_{500}$) is denoted Y_{500} (Y_{5R500}).Thus, as defined here, Y_{500} and Y_{5R500} have units of solid angle, e.g., arcmin^2.

3.2. Reference extraction method (Matched Multi-Filter, MMF3)

The ESZ sample is the result of a blind multi-frequency search in the all-sky *Planck*-HFI maps, i.e., no prior positional information on detected known clusters was used as input to the detection algorithm. The ESZ sample is produced by running the MMF3 algorithm, which is an all-sky extension of the matched multi-frequency filter algorithm described in Melin et al. (2006), over the six HFI frequency maps. The spectral distortion of the CMB due to the ICM can in principle be detected down to the lowest frequencies at which *Planck* operates; however, the beam at the lowest frequencies is large compared to typical cluster

[2] http://healpix.jpl.nasa.gov/ (Górski et al. 2005)

[3] In the following and unless otherwise stated, μK refers to equivalent CMB temperature fluctuations in μK.

[4] '*Planck* Sky Model', http://www.apc.univ-paris7.fr/APC_CS/Recherche/Adamis/PSM/ psky-en.php

[5] More details on the pressure profile can be found in Planck Collaboration (2011c)

sizes. Since clusters at moderate redshifts typically span angular scales of $\sim$ 5arcmin, the large beam of *Planck* at the LFI bands results in beam dilution of the SZ signal. The inclusion of the lowest *Planck* frequencies using the current algorithm therefore results in a lower S/N for the detected sources than if only the HFI bands were used. This reduces the efficiency of SZ cluster detection, which can potentially be improved in the future with refinements to the algorithm. As a consequence, for the generation of the ESZ list, only the *Planck* all-sky maps at frequencies of 100 GHz and above are considered.

The MMF algorithm, studied extensively by Herranz et al. (2002) and Melin et al. (2006), enhances the contrast, and thus S/N, of objects of known shape and known spectral emission profile over a set of observations containing contaminating signals. In its application for SZ, the method makes use of the universal frequency dependence of the thermal SZ effect. The filter optimises the detectability using a linear combination of maps (which requires an estimate of the statistics of the contamination) and uses spatial filtering to suppress both foregrounds and noise (making use of the prior knowledge of the cluster profile). The filter optimises cluster detection but it is not immune to contamination by false, non-SZ, detections which calls for an extensive validation procedure described in Section 4.

MMF3 first divides the all-sky maps into a set of 504 overlapping square patches of area 10×10 square degrees. Holes in the maps due to unsampled or badly sampled pixels are identified to construct an effective detection mask and are then filled in with the median value of the adjacent pixels. The matched multi-frequency filter then combines optimally the six frequencies of each patch assuming the SZ frequency spectrum and using the reference pressure profile presented in Section 3.1.

Auto- and cross-power spectra used by MMF3 are directly estimated from the data and are adapted to the local instrumental noise and astrophysical contamination. For each patch, the position and the scale radius (chosen to be $5R_{500}$) of the cluster profile, i.e., the cluster size $5\theta_{500}$, are varied to maximise the S/N of each detection. The algorithm hence assigns to each detected source a position, an estimated cluster size, $5\theta_{500}$, and an integrated Compton parameter, Y_{5R500}. In the present article and unless otherwise stated the *measured* integrated Compton parameter, noted Y_{5R500}, is thus computed by integrating the GNFW profile within a sphere of $5R_{500}$[6] encompassing most of the SZ signal. The detected sources extracted from the individual patches, with their assigned sizes and integrated Compton parameters, are finally merged into an all-sky cluster list. In practice the MMF3 algorithm is run in an iterative way; after a first detection of the SZ candidates, consecutive runs centred on the positions of the candidates refine the estimated S/N and candidate properties. At this stage, the uncertainty on Y_{5R500} is provided and takes into account the uncertainty in the cluster size estimate. The MMF3 algorithm can also be performed with fixed cluster size and position to estimate the SZ signal. This version of the algorithm was used to measure the integrated Compton parameters of known X-ray clusters in the ESZ sample, as explained in Section 6.2.

In order to address contamination by point sources, MMF3 uses a built-in source detection algorithm to reject point sources with S/N above ten which are then masked. This step avoids most of the false SZ detections associated with point sources. However, some residual contamination by non-SZ sources captured by the MMF3 algorithm may still be present and requires additional validation of the detection candidates (see Section 4).

[6] In the spherical assumption with this profile, Y_{500} the integrated Compton parameter within R_{500} relates to Y_{5R500} by $Y_{5R500} = 1.81 \times Y_{500}$.

3.3. Other extraction methods

The two other "direct" SZ detection methods used to confirm the blind detections of the ESZ candidates by MMF3 are discussed below. These methods previously compared rather well to each other within the SZ challenge match in terms of the detection properties (especially for high S/N sources). Their estimated sizes and SZ signals agree on average as well, though they differ on a case by case basis.

3.3.1. The Matched Multi-Filter Method, MMF1

The MMF1 algorithm is a completely independent implementation of the multi-frequency matched filter integrated within the *Planck*-HFI pipeline and infrastructure. A more detailed description of MMF1 is given in Melin et al. (2011). The full-sky *Planck* frequency maps are divided into 640 flat patches, each 14.66 degrees on a side (corresponding to 512 by 512 pixels), with overlapping regions of six degrees. The performance of the MMF algorithm is extremely sensitive to the quality of the estimated auto- and cross-power spectra of the background component in each frequency map. The size of the patches thus needs to be large enough to ensure a representative assessment of the background. The large overlap between patches was chosen so that all detections in a two-degree border around the edge of the patch may be discarded.

The detection of the SZ-candidates is performed on all the patches, and the resultant sub-catalogues are merged together to produce a single SZ-candidate catalogue. Similarly to MMF3, the candidate size is estimated by filtering the patches over the range of potential scales, from point-source sized objects and larger, and finding the scale which maximises the S/N of the detection of the candidate. In the version used on the *Planck* data, when merging sub-catalogues produced from the analysis of individual patches, it is also the S/N of the detection which is used when deciding which detection of the candidate is kept.

3.3.2. PowellSnakes (PwS) for SZ

PowellSnakes (PwS) is quite different from the MMF methods. It is a fast Bayesian multi-frequency detection algorithm designed to identify and characterise compact objects buried in a diffuse background. The detection process is grounded in a statistical model comparison test where two competing hypotheses are compared: the detection hypothesis and the null hypothesis. The statistical foundations of PwS are described in Carvalho et al. (2009).

Similarly to the MMF algorithms, a template parameterised SZ pressure profile is assumed known and representative of the majority of the cluster population observable with the resolution and noise characteristics of the instrumental setup. According to our data model, the pixel intensities result from the contribution of three independent components: the SZ signal, the astronomical background component, and the instrumental pixel noise. The last is assumed to be a realisation of a homogeneous stationary Gaussian random white noise process. The background astronomical components and the pixel noise are assumed uncorrelated and can each be modelled locally by a homogeneous Gaussian process.

The algorithm starts by minimising the model's likelihood ratio with respect to the model's parameters by using a Powell minimiser iteratively one source at a time. We assume that the sources are well separated and the fields not too crowded. The parameter estimation and the acceptance/rejection threshold is

defined using Bayesian approach with priors adjusted on the *Planck* Sky Model SZ Catalogue.

PwS performs on flat 512×512 pixel patches of 14.66 degrees on a side. When applying a Galactic cut of $|b| > 14$ degrees, PwS splits the sphere into 2324 patches. However, only detections lying inside the inner 256×256 pixels are considered. So, on average PwS detects each cluster more than three times (usually four times), increasing the reliability of the detection. The selection of the candidate detection that goes into the final catalogue uses the Bayesian mode of PwS, based on the highest ratio of model posteriors.

4. Validation of the ESZ sample

The SZ validation process, Fig. 2, is an integrated HFI-LFI effort within *Planck* Working Group 5 (WG5[7]) "Clusters and Secondary anisotropies". It has been established in order to validate the full SZ candidate lists obtained from the extraction methods developed by the *Planck* collaboration. It relies mainly on a three-stage process detailed in the following subsections:

- **Internal validation** steps based on *Planck* data:
  - search for and rejection of associations with SSOs and artefacts;
  - rejection of sources with rising spectral energy distribution in the high HFI frequency bands;
  - cross-check with other *Planck* source catalogues to reject SZ candidates identified with cold cores (CC) and other Galactic sources; and
  - redundant detections of the same candidates by methods other than the reference one.
- **Candidate identification** steps based on ancillary data:
  - identification of SZ candidates with known clusters from existing X-ray, optical/near infrared (NIR), and SZ catalogues and lists; and
  - search in NED and SIMBAD databases.
- **Follow-up programmes** for verification and confirmation of SZ candidates.

4.1. Construction of ESZ sample and internal validation

The construction of the ESZ list of SZ candidates starts with the blind detection of candidates using the implementation of the MMF3 algorithm at the US Planck Data Center applied to *Planck*-HFI channel maps at Galactic latitudes $|b| > 14$ deg. A total of about 1000 blind SZ candidates are detected with S/N ≥ 4. As discussed above, the MMF3 algorithm uses prior information on the SZ spectrum and on the cluster shape. However, especially due to the beam-sizes of the order of a few arcminutes, the resulting list of SZ candidates is not immune from false detection due mainly to dust emission at high frequencies from the interstellar medium (ISM) or infrared sources, and very moderately to the CMB fluctuations at low frequencies (see illustrations of channel maps in upper panels of Fig. 5). In the following, we do not explicitly check for association with extragalactic point sources emitting at *Planck*-HFI frequencies, which is essentially dealt with internally by the MMF3 algorithm (Sect. 3.2). Some residual contamination of the SZ Compton Y parameter by point sources may, however, still be present (see Section 6.4 for a specific discussion).

The internal validation process starts by removing spurious detections from the output list of blind SZ candidates, which is achieved in two steps. We first reject the candidates showing rising spectral energy distributions in the highest *Planck*-HFI frequency bands. They represent around 14% of the initial blind SZ candidates. Second, the remaining blind SZ candidate sample is further cleaned by rejecting all objects associated with either Galactic sources, or CC detected using the CoCoCodet algorithm (Montier et al. 2010; Planck Collaboration 2011f) within a 7 arcmin radius of SZ candidates. This step further reduces the sample of remaining SZ candidates by about 17%.

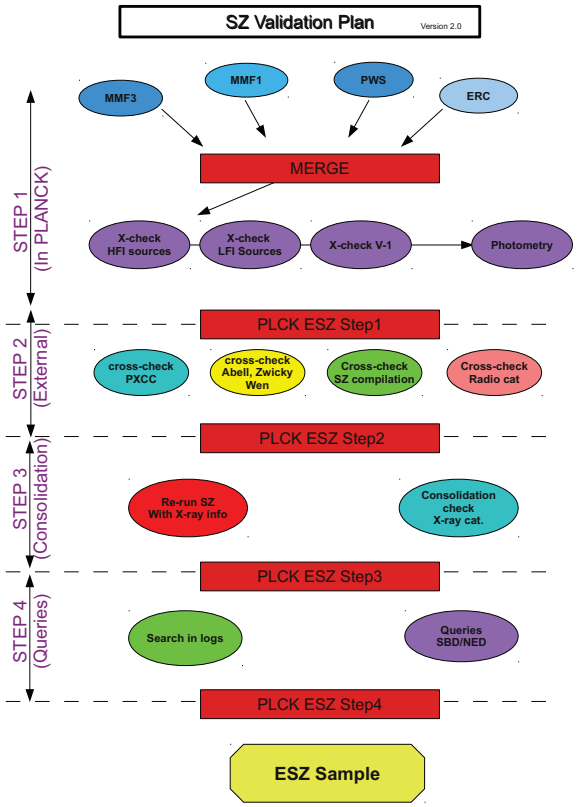

Fig. 2. Flowchart of the SZ validation process applied to the *Planck* cluster sample.

After this two-step process, the initial blind SZ candidate sample has been reduced to around 770 blind SZ candidates with S/N ≥ 4. However at this S/N level many candidates will not correspond to actual clusters. Theoretical predictions based on the PSM simulations indicate that the purity (ratio of true to all detections) is expected to be of the order of 70% at S/N = 4 (Fig. 15). The simulations do not account fully for the complexity of the true sky nor for the inhomogeneity of the noise across the sky. The actual purity is thus likely to be worse than the prediction. In order to ensure a high level of purity in the ESZ sample and based on lessons learnt from the XMM-Newton observations of low S/N candidates (see Planck Collaboration (2011b)), an early decision was made to cut at a higher S/N level of S/N ≥ 6 for this first *Planck* data release. This more stringent condition retains 201 SZ cluster candidates. Taking advantage of the outcome of the follow-up programme for cluster confirmation by XMM-Newton, we further retain only the SZ candidates detected blindly by the MMF3 algorithm *and* at least one other method, be it MMF1 or PowellSnakes. This results in 190 SZ cluster candidates; these constitute the baseline ESZ sample. A detailed inspection of the SZ maps and spectra of the 11

[7] http://www.ita.uni-heidelberg.de/collaborations/planck/

discarded SZ candidates was performed (see Section 5.2.2) and confirmed that these sources were false detections.

A final internal check consisted of searching for associations of the obtained 190 SZ candidates with possible artefacts such as low-frequency noise stripes, ringing from neighbouring bright sources, hot pixels, non-observed pixels or poorly sampled pixels in the vicinity of SSO-flagged regions. None of the 190 ESZ candidates was associated with such artefacts.

4.2. Candidate identification with ancillary data

The second stage of the SZ validation process consisted of cross-matching the obtained list of 190 blind SZ candidates with external cluster catalogues in X-rays, optical and SZ domains. This allowed us to identify the SZ candidates associated with previously known clusters and consequently isolate the *Planck* candidate new clusters.

4.2.1. With X-ray cluster catalogues

For the association of *Planck* SZ candidates from the blind extraction with known X-ray clusters, we have used the Meta-Catalogue of X-ray detected Clusters of galaxies (MCXC, Piffaretti et al. 2010). This homogenised compilation of X-ray detected clusters of galaxies comprises approximately 1800 clusters from publicly available ROSAT All Sky Survey-based (NORAS, REFLEX, BCS, SGP, NEP, MACS, and CIZA) and serendipitous (160SD, 400SD, SHARC, WARPS, EMSS, etc) cluster catalogues.

For each X-ray cluster in the MCXC several properties are available, amongst which are the X-ray centroid coordinates, redshift, identifiers, and L_{500}.[8] The luminosities are adopted as proxies to estimate the total mass M_{500} using the L–M relation from REXCESS (Pratt et al. 2009), and radius R_{500}, and to predict the integrated Compton $Y^{L_X}_{5R500}$, or alternatively $Y^{L_X}_{500}$, as detailed in Planck Collaboration (2011c) as well as other *Planck*-related quantities.

Because the MCXC compilation includes only clusters with available luminosity (redshift) information, we supplement it with about 150 clusters where this information is missing. This implies that for the latter only centroid positions are available. The resulting meta-catalogue, for simplicity referred to as MCXC in the reminder of the article, is extensively used during the external validation process. For a given *Planck* candidate cluster we identify the closest MCXC cluster. The reliability of the association is checked based on the distance, as compared to the cluster size, and on the measured Y_{5R500} (or S/N) values, as compared to the expected values $Y^{L_X}_{5R500}$ (or S/N) for the MCXC clusters.

4.2.2. With optical cluster catalogues

The baseline for the identification of blind SZ candidates from the ESZ with clusters known in the optical is the cross-match with the Abell cluster catalogue (Abell 1958, 5250 clusters of which 1026 have a redshift) and the Zwicky cluster catalogue (Zwicky et al. 1961, 9134 objects). The association criterion here was a positional match with a search radius for both catalogues set to five arcminutes.

Furthermore, the ESZ sample was cross-checked against the MaxBCG (Koester et al. 2007) and Wen et al. (2009) catalogues with a search radius of 5 arcmin.

4.2.3. With known SZ clusters

The identification of SZ candidates is also performed at millimetre wavelengths by cross-matching the SZ candidate list with a compilation of SZ observed galaxy clusters from the literature undertaken by Douspis et al. (in prep.). This compilation is based on SZ observations conducted with the numerous experiments developed during the last 30 years (Ryle, OVRO, BIMA, MITO, Nobeyama, SZA, APEX-SZ, AMI, Diabolo, Suzie, Ryle, AMIBA, ACBAR, etc). It also includes the new clusters recently discovered through their SZ signature by ACT and SPT. In total the compilation comprises 111 SZ clusters including 28 newly discovered by ACT and SPT (Menanteau et al. 2010; Vanderlinde et al. 2010). The association of the *Planck* SZ candidates was based on positional matching with a search radius of five arcminutes.

4.2.4. Queries in SIMBAD and NED databases

The information provided from querying databases is mainly redundant with cross-checks with cluster catalogues in X-ray or optical. However, running both cross-matches is important to avoid missing a few associations. It is also important to retrieve the information on redshifts for those identified clusters not included in the MCXC. We therefore performed a systematic query in SIMBAD. The adopted search radius was set to five arcminutes. For NED, no systematic query was implemented. Cluster candidates within the same search radius were rather checked against a list of objects retrieved from NED flagged as "Clusters of galaxies". Finally the candidates were also checked against the X-ray cluster database (Sadat et al. 2004, BAX:).

4.3. Follow-up programme for validation and confirmation

In parallel to the effort of SZ candidate cross-identification, a coherent follow-up programme targeted towards the verification/validation of the cluster candidates in the SZ catalogue was put into place in the form of an internal roadmap. The main goals of this follow-up programme are to confirm *Planck* candidates as new clusters, and as a consequence to better understand both the SZ selection criteria in the *Planck* survey and the reliability of selected sources.

Considering the complementarity of X-ray, optical and IR/SZ, observational follow-ups have been coordinated to optimise the validation and the understanding of the *Planck* selection. In practice, this took the form of a confirmation programme relying on observations with XMM-Newton[9] making use of Director Discretionary Time (DDT) as detailed in Planck Collaboration (2011b). This is complemented by observations in the optical using the European Northern Observatory facilities (ENO), the European Southern Observatory 2.2m-telescope, and two pilot programmes, one with the WISE experiment (Wright et al. 2010) for the search of overdensities in the IR data, and one with the Arcminute MicroKelvin Imager[10] (AMI, Zwart et al.

[8] The X-ray luminosities as measured within an aperture of radius R_{500}

[9] *XMM-Newton* is an ESA science mission with instruments and contributions directly funded by ESA Member States and the USA (NASA)

[10] AMI is a pair of interferometer arrays located near Cambridge, UK, operating in six bands between 13.5 and 18 GHz, with sensitivity to angular scales 30 arcsec – 10 arcmin.

(2008)) for the confirmation of *Planck* candidates with SZ observations.

An ensemble of SZ candidates spanning a range of S/N between four and eleven was selected from earlier versions of the HFI channel maps and sent to the above-mentioned facilities. The targets were selected from a list of SZ candidates after the external validation stage (i.e., identification of known clusters). They went through visual inspection of their maps and spectra produced by all the available methods described in Section 5.2.2. Furthermore, in order to avoid duplicating existing observations of candidates with the same or similar facilities, the cluster candidates were further cross-matched with logs of X-ray, optical, and NIR observatories.

The search in X-ray observatories (ROSAT, Suzaku, XMM-Newton, and Chandra) was performed using the HEASARC tool.[11] For XMM-Newton and Chandra both master catalogues and accepted GO (Guest Observer) targets were used in the search. For Suzaku, only the master catalogue was used. In the case of optical and NIR observatories, the search was performed in the public logs of several optical/infrared observatories. In some cases, this search was completed using VO (Virtual Observatory) tools[12]. The checked resources were: ING Archive, UKIRT Archive, ESO Archive, HST Archive (at ESO), CFHT Archive, AAT Archive, NOAO Science Archive, Multimission Archive at STScI (MAST), Gemini Science Archive, and SMOKA (Subaru Mitaka Okayama Kiso Archive). In addition, a search in the footprint of the covered area for known surveys was performed. The searched areas considered were those of SDSS, UKIDSS, and HST (ACS-WFC) as they are described in the VO footprint service[13] (Budavári et al. 2007), as well as those of SPT and ACT experiments.

The details and results of the confirmation follow-up with XMM-Newton are given in Planck Collaboration (2011b). A total of 25 targets were observed with short snapshot exposures (i.e., 10 ks nominal EPN) out of which 21 were confirmed as clusters or systems of multiple extended X-ray sources (i.e., double or triple). Complying with *Planck* policies and following the agreement between the *Planck* and XMM-*Newton* ESA project scientist, all the data are made public with the publication of the *Planck* early results and the *Planck* ERCSC. Of the 21 confirmed *Planck* SZ sources, 11 are found in the ESZ sample and are discussed in Section 5.2.1. The remaining clusters with S/N < 6 are discussed in Planck Collaboration (2011b). One candidate cluster in the ESZ sample was confirmed by AMI and WISE. None of the targets sent for observation in the optical with the ENO telescopes met the ESZ selection criteria.

5. Results of the validation

In the following we will detail the outcome of the external validation of the 190 SZ candidate clusters retained after the internal validation. We find that they are distributed between known clusters (169 in total, Fig. 3 blue) and 21 candidate new clusters. Among those 21, twelve have been confirmed (Fig. 3 yellow) and these are discussed in Section 5.2.1. Nine remain as candidate new clusters requiring confirmation (Fig. 3 red); they are described in Section 5.2.2. The further checks performed on the candidate new clusters resulted in the rejection of one of the nine candidates.

[11] http://heasarc.gsfc.nasa.gov/cgi-bin/W3Browse/w3browse.pl
[12] VO command line tools http://iraf-nvo.noao.edu/vo-cli/
[13] http://www.voservices.net/footprint

The final released ESZ list thus comprises 189 clusters or candidate new clusters. The content of the released data[14] is presented in Appendix A.3. Table 1 summarises the different steps of ESZ sample construction and validation detailed in the previous sections. Figures 5 and 6 show illustrations of the raw and "cleaned" channel maps (from 100 to 545 GHz) as well as corresponding *y*-maps, for a few clusters, with S/N ranging from the highest ones to more typical ones.

5.1. ESZ candidates identified with known clusters

The external validation with ancillary data identified 169 clusters in total out of the 190 candidates detected blindly. They are known X-ray or optical clusters and *Planck* data provide the first measure of the SZ signal for the majority of them, opening a new observational window on those already known objects.

Most of the identified SZ candidates, 162 in all, were associated with known clusters from the MCXC compilation and 158 have known redshifts (provided in the compilation), X-ray luminosities, X-ray estimated sizes (θ_{500}), etc. Moreover, as expected, a very large fraction of them (127 clusters) are at the same time identified in the optical. They are mostly Abell clusters from the ROSAT X-ray cluster catalogues.

The remaining seven identified *Planck* clusters were obtained from search in SIMBAD (one cluster, RXJ0748.7+5941, observed by ROSAT but not part of the NORAS catalogue (Appenzeller et al. 1998) and without published redshift), from logs of observatories (one cluster, H1821+643 at $z = 0.299$ (Schneider et al. 1992)) and from optical only, i.e., without an X-ray counterpart, identification with Abell or Zwicky clusters (five clusters). These are ZwCl2120.1+2256, AC114Northern, A3716S, ZwCl1856.8+6616, and ZwCl0934.8+5216 clusters. The last two have no published redshifts. For all these clusters, redshifts when they are available are retrieved from the SIMBAD and NED databases.

The cross-match with known SZ clusters further indicates that one cluster, AS0520, is common to *Planck*, ACT and SPT. Additionally, five[15] clusters from ACT are in common with the *Planck* ESZ sample, and twelve massive clusters observed by SPT (Plagge et al. 2010) are also observed by *Planck* and quoted in the ESZ. Finally by comparing with the SZ compilation from Douspis et al. (2011), we find that, in total, 41 clusters from the ESZ sample have already been observed in SZ by previous experiments. For these clusters *Planck* provides us with a homogeneous set of SZ measures. Moreover, out of the full ESZ sample about 80% have been observed in SZ for the first time and have a homogeneous measurement of their Compton parameter from *Planck*.

Out of the known clusters in the ESZ sample, a few are given in the Early Release Compact Source Catalogue (ERCSC) (Planck Collaboration 2011g) as they were detected by the source extraction techniques used to construct the ERCSC. They are 1ES 0657-55.8 (commonly known as the bullet cluster and detected blindly with an S/N of 19.7), A2218, ACO S0520, CIZA J1938.3+5409, A0119, RXC J1720.1+2637, A3376, and MACS J2135.2-0102. It is worth noting that the quoted fluxes in the ERCSC are obtained using aperture photometry on the

[14] *http://www.rssd.esa.int/Planck*
[15] One of the candidate new clusters confirmed by XMM-*Newton* appeared in publication as one of the ACT SZ optically-confirmed clusters (Menanteau et al. 2010) to be observed by *Chandra*, after we scheduled it for observation with XMM-*Newton*: PLCKESZ G262.7-40.9/ACT-CL J0438-5419. We retain it as new candidate in the following.

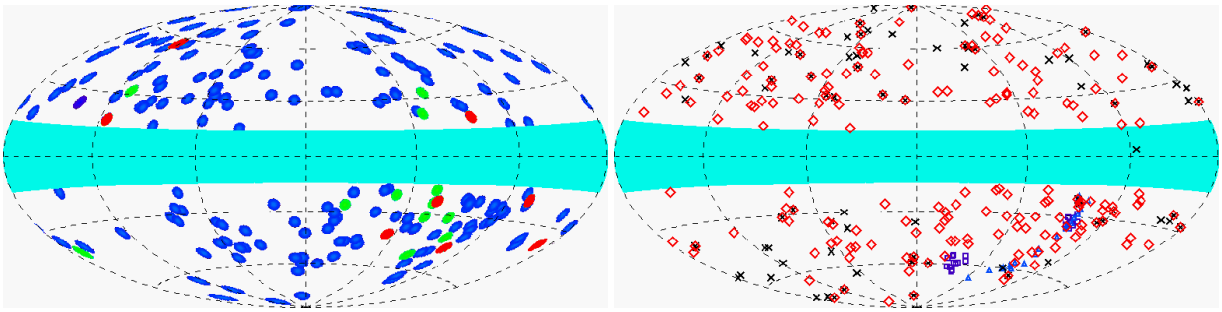

Fig. 3. Distribution of ESZ clusters and candidate clusters on the sky (Galactic Aitoff projection). Left panel: In blue are ESZ clusters identified with known clusters, in green the ESZ confirmed candidates, and in red the ESZ candidate new clusters yet to be confirmed. Right panel: In red diamonds the ESZ sample, in black crosses the compilation of SZ observations prior to 2010, in dark blue triangles ACT clusters from Menanteau et al. (2010), and in purple squares SPT clusters from Vanderlinde et al. (2010). The blue area represents the masked area of $|b| < 14$ deg.

Table 1. Summary of the ESZ sample construction and validation steps.

Selection		SZ Candidates	Rejected
	S/N $\geq$ 6 and good quality flag on SZ spectrum	201	
	Detected by one method only		11
	Bad quality flag from visual inspection		1
ESZ sample		189	
Known clusters		169	
	X-ray only	30	
	Optical only	5	
	NEDSimbad only	1	
	X-ray + Optical	128	
	X-ray + SZ	1	
	SZ + Optical	1	
	X-ray + Optical +SZ	3	
New *Planck* clusters		20	
	XMM confirmed	11	
	AMI confirmed	1	
	Candidate new clusters	8	

channel maps without band merging. They cannot be compared easily with the obtained integrated Compton parameters in the present article. Moreover, two of the above-listed clusters, RXC J1720.1+2637 and MACS J2135.2-0102, suffer from astrophysical contamination that may affect the computed Y.

5.2. New Planck clusters in the ESZ sample

The ESZ sample contains 20 new clusters or candidates clusters with S/N ranging from 11.5 to 6. As mentioned above, a follow-up programme set up to help understand the selection of *Planck* clusters allowed us to confirm 12 clusters. Eleven were confirmed with XMM-Newton snapshot observations, while one cluster was confirmed with AMI observations and corresponds to an overdensity of galaxies in the WISE data.

5.2.1. Confirmed ESZ cluster candidates

The XMM-Newton observations for confirmation of SZ candidates were based on earlier versions of the channel maps and an earlier version of the data processing than that used for the ESZ construction. The 25 targets sent for observation were selected in two different campaigns, a pilot programme (exploring S/N from six down to four) and a higher S/N programme (above S/N of 5). Among the 21 *Planck* cluster candidates confirmed by snapshot observation with XMM-Newton, 11 clusters have a *Planck* S/N above six (in the present map version) and thus meet the ESZ selection criteria. Two of them were found to be double clusters on the sky. All eleven are published in the ESZ release. Together with the remaining ten clusters confirmed by XMM-Newton, all are described in Planck Collaboration (2011b). In the following we just summarise the general properties of the new confirmed clusters in the ESZ.

The eleven new clusters in the ESZ confirmed by XMM-Newton have S/N ranging from 11.5 to 6.3. They were found to lie below the REFLEX flux limit of 3×10^{-12} erg s^{-1}, except for two confirmed clusters above the limit. These clusters happen to have associations with BSC sources and to be situated above the MACS limit; however their redshifts, $z = 0.27$ and $z = 0.09$ are below the considered redshifts for MACS [see the detailed discussion in Planck Collaboration (2011b)]. The redshifts of the new confirmed clusters were estimated directly from X-ray observations of iron emission lines, and range between $z = 0.2$ and 0.44. Only two out of the eleven confirmed new clusters have optical redshift estimates. For one new cluster (PLCKESZ G285.0-23.7), the agreement between the X-ray estimated and photometric redshifts is quite good. The second cluster, PLCKESZ G262.7-40.9, was found to be an ACT cluster, published after the scheduling of XMM-Newton observation, for which there is a discrepancy between the X-ray-estimated redshift ($z = 0.39$) and the photometric redshift ($z = 0.54$) from Menanteau et al. (2010). The range in temperature spanned by the new confirmed clusters in the ESZ is from about 4 to 12 keV, and the derived

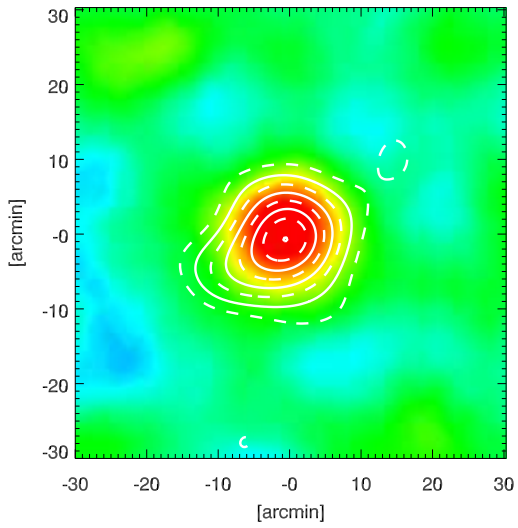

Fig. 4. y-map of PLCKESZ G139.59+24.19 as observed by *Planck* (colour image) and AMI (contours) at a common resolution of 13 arcmin. The contours are from two to nine in S/N ratio.

masses range from about 4 to $15 \times 10^{14} M_{\odot}$. Three new clusters in the ESZ sample have masses of $10 \times 10^{14} M_{\odot}$ or above, including the most massive cluster detected by *Planck* with a mass of about $15 \times 10^{14} M_{\odot}$. The confirmation of the *Planck* new clusters by XMM-Newton provides us with positions and, most of all, a better estimate of the cluster size that will be important for the re-extraction of Y values (see Section 6.2).

One additional candidate cluster, PLCKESZ G139.59+24.19 detected at S/N = 7.2, was confirmed by a pilot project for confirmation with the AMI interferometer (see Fig. 4 showing the *Planck* y map with the AMI contours, obtained after the subtraction of bright sources with the large array observations, overlaid). The *Planck* cluster was detected at 9σ by AMI in a long-time exposure of approximately 30 hours. Preliminary results from AMI give an integrated Compton parameter of $Y_{5R500} = (17.0 \pm 1.7) \times 10^{-4}$ arcmin^2, extracted fixing the cluster size to the estimated size from *Planck*. The *Planck* value, $Y_{5R500} = (32 \pm 13) \times 10^{-4}$, is obtained from the blind detection of the cluster. The error bar takes into account the uncertainty in the cluster size estimate by the MMF3 algorithm. A detailed comparison is planned. This same cluster was also confirmed at a S/N level of five by WISE.

5.2.2. ESZ candidate new clusters

A closer inspection of the ESZ candidate new clusters was performed in order to ensure the reliability of the retained candidate new clusters. The same close inspection was also performed, a posteriori, in order to confirm the rejection of the 11 candidates excluded in the final steps of the ESZ construction because they were observed solely by MMF3 (Sect. 4.1). This closer inspection of the candidates was based on both internal (using *Planck* alone) and external data.

For the in-depth inspection of the *Planck* data, we used cleaned channel maps, reconstructed y-maps and SZ spectra. All these products are quite sensitive to the procedure used for cleaning the channel maps, i.e., to the component separation method. We therefore simultaneously employed different cleaning approaches developed by the *Planck* collaboration, briefly described below, in order to ensure convergence and redundancy in the derived conclusions. One of the methods is based on the construction of SZ y-maps centred on the ESZ candidate positions using the Modified Internal Linear Combination Algorithm (MILCA, Hurier et al. (2010)) applied independently on each SZ-centred patch. The contribution from other sources of sky emission such as thermal dust and radio and infrared sources is thus more accurately reduced. Other approaches based on local component separation and aperture photometry were also developed in order to check the y-maps and SZ spectra of the candidates. Patches centred on the SZ candidates are produced from the *Planck* channel maps and the IRIS map (Miville-Deschênes & Lagache 2005). Local component separation is performed by decorrelating from the low-frequency channels an extrapolation of the dust emission computed with the 857 GHz and IRIS maps. The "dust-free" 217 GHz map is then removed from all channels and visual inspection can then be performed on these cleaned patches. From this set of maps we then obtain SZ reconstructed y-maps and an SZ spectrum by applying aperture photometry to each patch. The internal inspection of the *Planck* data (y-maps, frequency maps and spectra) therefore provides us with a set of quality flags that were used for the selection of targets for the follow-up programmes and that are used for a qualitative assessment of the reliability of the candidates.

Converging negative quality assessments result in the rejection of the SZ candidates. However in most cases, it is useful to combine and complement the *Planck*-internal quality flags with external information. In practice this consists in searching for associations with FSC (Faint Source Catalogue) and BSC (Bright Source Catalogue) RASS sources, searching in, and visualising, the RASS maps at the candidate cluster positions, and finally performing visual checks of the DSS (Digital Sky Survey) images in the candidate field (within a five arcminute radius from the *Planck* position). Based the lessons learnt from the XMM-Newton confirmation programme, the association of candidates with FSC or BSC-RASS sources (in the five arcminute radius field) was considered as an indication of the reliability of the candidate. The presence of an excess in the count-rate RASS images in the candidate field was also used as a reliability flag. The DSS images were used simply as an "empirical" assessment of the presence of an overdense region. It is worth noting that the external information provided in particular by the RASS data never supersede the *Planck*-internal quality flags. As a matter of fact, two of the confirmed new clusters had neither FSC nor BSC associations. Conversely, associations with FSC and BSC-RASS sources were found for SZ candidates that turned out to be false detections (Planck Collaboration 2011b).

Using the internal quality flags and the additional external checks, out of the nine candidate new clusters retained by the ESZ construction, seven were judged reliable. Two candidate new clusters had rather poor quality flags and no external associations. One of them was found to be associated with dust cloud emission. Note that this source was not flagged by the cross-match with the CC and Galactic sources, nor identified with a rising spectral distribution at high frequencies during the internal validation and ESZ construction. This candidate was rejected from the final ESZ sample, reducing the total number of clusters and candidate clusters from 190 to 189. The second cluster candidate with low reliability (PLCKESZ G189.84-37.24), was kept in the ESZ list as it was not associated clearly with any non-SZ

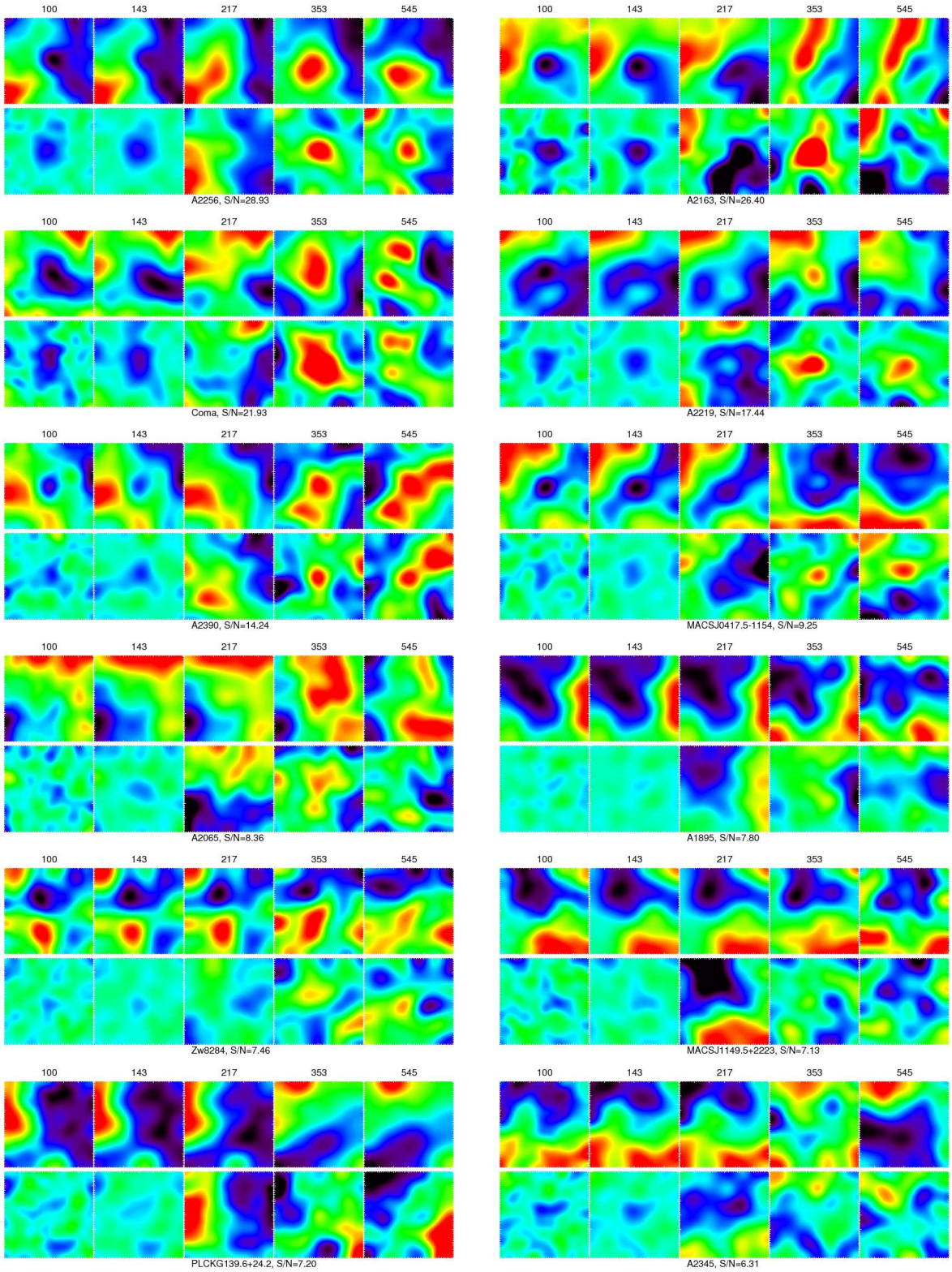

Fig. 5. Observations of a few clusters from the ESZ sample. For each cluster, the upper panels show the raw (1 square degree) maps at 100, 143, 217, 353, and 545GHz. The lower panels show the corresponding cleaned maps (see Sect. 5.2.2). These clusters span S/N from 29 to 6 from the upper left to the lower right.

source. Table 2 summarises the external information associated with the candidate new clusters in the ESZ sample[16].

[16] During the review process 6 of the 8 *Planck* cluster candidates were confirmed by SPT (Story et al. 2011; Williamson et al. 2011) and AMI (Hurley-Walker et al. 2011) experiments independently of the *Planck* collaboration.

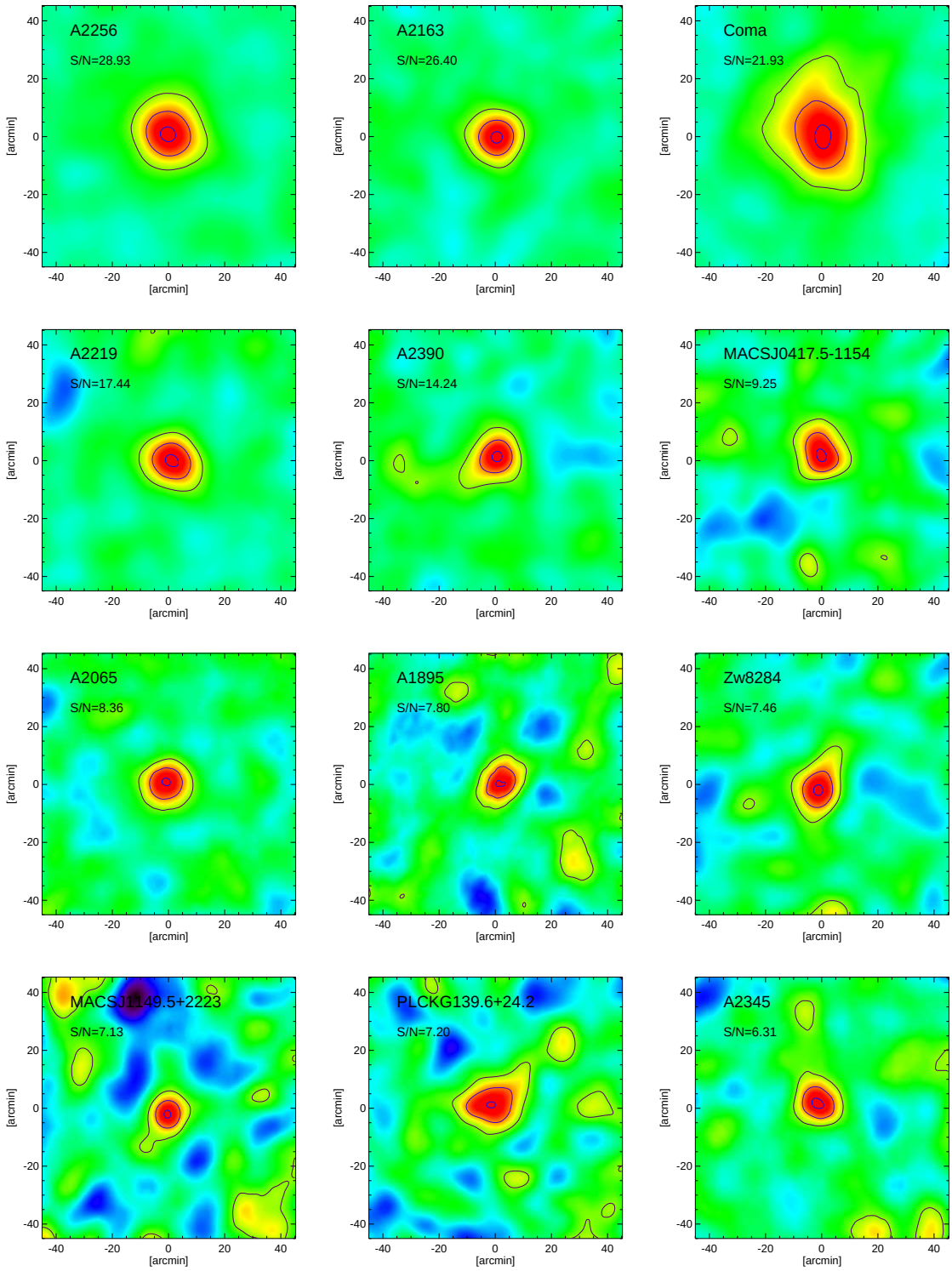

Fig. 6. Illustrations of reconstructed *y*-maps (1.5° × 1.5°, smoothed to 13 arcmin) for clusters spanning S/N from 29 to 6 from the upper left to the lower right.

6. Error budget on the cluster parameters

6.1. Position

The ESZ sample contains a list of 189 clusters or candidate clusters distributed over the whole sky with positions obtained from blind detection with the MMF3 algorithm. Based on the simulation used for the SZ challenge comparison, we find that MMF3 recovers cluster positions to ∼ 2 arcmins on average. However, there is a large scatter in the positional accuracy, as seen in Fig. 7.

For the 158 ESZ candidates identified as X-ray clusters with known X-ray size, the coordinates of the X-ray counterpart are given by the MCXC. The X-ray position is also given for the *Planck* cluster candidates confirmed by XMM-Newton as single objects. The comparison of the SZ candidate positions derived

Table 2. For the *Planck* candidate new clusters not yet confirmed at the time of submission, external information from RASS.

Name	RASS association	Distance to source (arcmin)	S/N of RASS source	S/N of RASS in *Planck* aperture	Note
PLCKESZ G115.71+17.52	BSC	0.17	8.7	8.5	Possible contamination by dust emission
PLCKESZ G121.11+57.01	FSC	1.72	2.9	4.1	Possible association with WHL J125933.4+600409 from Wen et al. (2009), $z = 0.33$
PLCKESZ G189.84-37.24	None	-	-	1.3	Low reliability, high level of contamination by Galactic emission
PLCKESZ G225.92-19.99	FSC	1.11	2.5	6.7	With XMM-Newton and HST pointed observations
PLCKESZ G255.62-46.16	FSC	0.9	2.7	3.8	With ESO and Suzaku pointed observations
PLCKESZ G264.41+19.48	BSC	1.22	4.6	5.7	
PLCKESZ G283.16-22.93	FSC	0.54	3.6	4.2	
PLCKESZ G304.84-41.42	BSC	0.55	3.6	5.1	With ESO pointed observations

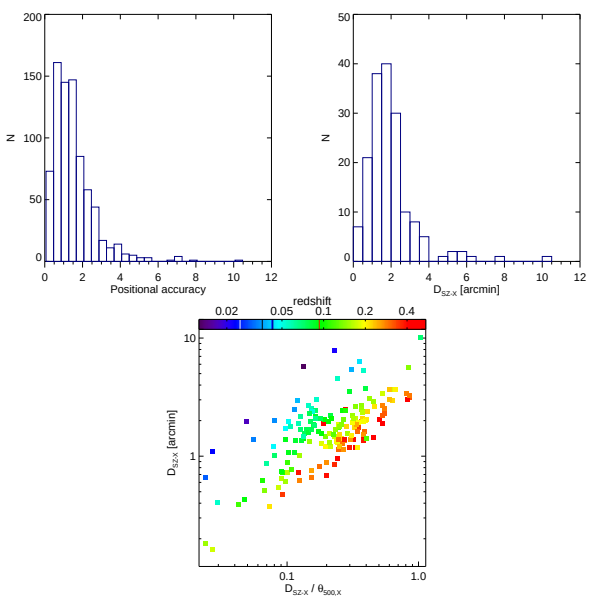

Fig. 7. Upper left panel: Positional accuracy from MMF3 based on simulations for the SZ challenge. Upper right panel: Distribution of the distance between the SZ blind position and the X-ray position ($D_{\rm SZ-X}$) for 167 known, or confirmed with XMM-Newton, X-ray clusters. Lower panel: Separation of the SZ blind and X-ray positions $D_{\rm SZ-X}$ as a function of $D_{\rm SZ-X}$ normalised to the cluster size $\theta_{500,\rm X}$.

from the blind detection with the X-ray positions of the identified or confirmed clusters for a total of 167 clusters is shown in Fig. 7, left panel. The positional offset between *Planck* blind and X-ray positions, $D_{\rm SZ-X}$, is of the order of 2 arcmin on average, consistent with the estimates obtained from the SZ challenge simulation. Very few clusters (8 in total over 167) have an offset $D_{\rm SZ-X} > 4$ arcmin, and stand out as clear outliers in the distribution. It is worth noting that such a positional offset combines both the uncertainty in the position reconstruction from MMF3 and the possible physical offset between the centroids of X-ray and SZ signals (e.g., in merging clusters). The eight clusters with $D_{\rm SZ-X} > 4$ arcmin are all nearby merging clusters or members of larger structures such as A3532 in the Shapley supercluster, or contaminated by radio source emission. The cluster A1066 ($z = 0.07$), which has the largest positional offset ($D_{\rm SZ-X} = 10$ arcmin), is in the Leo Sextans supercluster (Einasto et al. 2001). In addition, it may suffer from point source contamination. The cluster Abell 1367 at $z = 0.02$ with $D_{\rm SZ-X} = 7.8$ arcmin is a young cluster currently forming at the intersection of two filaments (Cortese et al. 2004) with complex gas density and temperature structures (Ghizzardi et al. 2010).

As seen from Fig. 7, right panel, large (greater than four arcmin) offsets are only seen in nearby clusters (seven out of the eight clusters with $D_{\rm SZ-X} > 4$ have redshifts lower than 0.08). They remain smaller than the cluster size, as expected for offsets dominated by physical effects. On average, the offsets tend to decrease with increasing redshift and seem to become independent of redshift above $z \sim 0.3$. This is due to the decreasing contribution of possible physical offsets, which become unresolved. The overall offset, including the absolute reconstruction uncertainty, remains smaller than the cluster size for most of the clusters in the ESZ θ_{500} (Fig. 7, right panel). However, we expect that it will be of the order of cluster size for clusters at higher redshifts than the range currently probed. This positional offset is therefore an additional source of uncertainty in the cluster position which needs to be taken into account in the follow-up observations for candidate confirmation.

6.2. Cluster size-*Y* degeneracy

The MMF algorithm, and more generally algorithms that are based on the adjustment of an SZ profile to detect clusters, generally perform better than algorithms which do not assume an SZ profile. The GNFW profile used in the present study corresponds to a shape function characterised by two parameters, the central value and a characteristic scale $\theta_{\rm s}$ (with $\theta_{\rm s} = \theta_{500}/c_{500}$ and c_{500} is the concentration parameter). Simulations showed that the intrinsic photometric dispersion of the recovered integrated Compton parameter, with a GNFW profile, could be of order 30% (see Fig. 8) even with the prior information on the pressure profile. This is due to the difficulty of estimating the cluster size, which in turn is degenerate with the SZ Y estimate.

This cluster size-Y degeneracy is illustrated, here using PwS, in two extreme situations (Fig. 9) showing the likelihood plots (integrated Compton vs cluster size) of an extended high S/N cluster such as Coma (blue contours) and an unresolved S/N = 6 cluster (black contours). In both cases, the integrated Compton parameter Y is highly correlated with the estimated cluster size. We find a correlation coefficient $\rho = 0.91$ and $\rho = 0.75$ for Coma and the "unresolved cluster" respectively. On average over the ESZ sample we find a correlation of $\rho = 0.85$. The degeneracy between cluster size and Y is extremely detrimental, as it will more than double the average fractional uncertainty relative to the Y value in the case where we knew the true value of $\theta_{\rm s}$

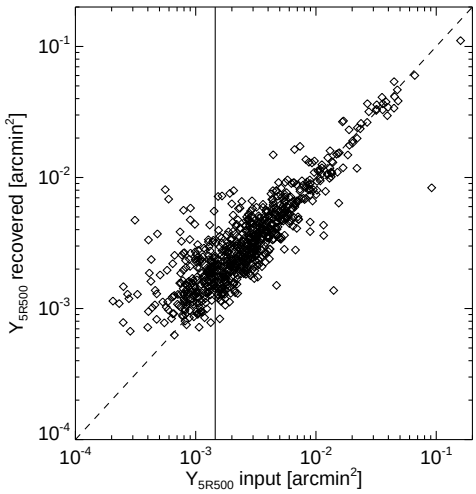

Fig. 8. Input versus recovered integrated Compton parameter from MMF3, based on simulations for the SZ challenge.

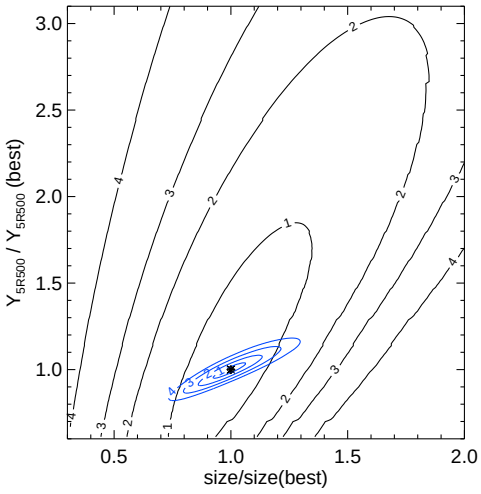

Fig. 9. Illustration of the cluster size-Y degeneracy from PwS. Shown are the cases of Coma cluster (high S/N and extended in blue), and that of an S/N = 6 unresolved cluster (in black). Parameters are plotted with respect to the best fit points in each direction.

perfectly. As a result, any attempt to constrain the cluster size (equivalently θ_s), fixing or assuming a prior for its value, brings a significant reduction on the Y value dispersion.

The issue of the cluster size-Y degeneracy is of particular importance in the case of *Planck*, for which a vast majority of clusters are only marginally resolved. This issue is also crucial when one wants to use the SZ signal as a mass proxy. Indeed, the dispersion in Y due to the cluster size-Y degeneracy is likely to dominate the intrinsic scatter of order 10% of this mass proxy (da Silva et al. (2004), Arnaud et al. (2007)).

As a result, we have re-estimated the integrated Compton parameter for all the ESZ candidates with prior information on their sizes. We have chosen the X-ray sizes (θ_{5R500}) derived from the X-ray luminosities, L_{500}, as detailed in Piffaretti et al. (2010), as suitable estimates of the cluster sizes. Using the MMF3 version implemented in HFI Core team and SZ validation team, Y_{5R500} were thus re-computed from the *Planck* channel maps

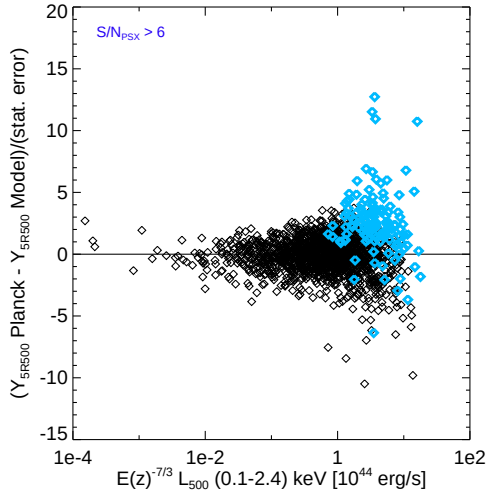

Fig. 11. Ratio of predicted vs observed Y_{5R500} for the MCXC clusters as a function of the X-ray luminosity L_{500} used to estimate the cluster properties (radius and integrated Compton parameter). The light-blue diamonds indicate a cut of 6 in predicted S/N corresponding to the ESZ selection criterion.

at fixed X-ray position and with imposed cluster size equal to the X-ray luminosity based θ_{5R500}. The integrated Compton parameter Y was re-estimated for all the clusters with known X-ray counterparts, being the 158 ESZ candidates identified with known clusters from the MCXC and the nine ESZ clusters confirmed by XMM-Newton as single objects.

Fig. 10, left panel, illustrates the effect of fixing the position and the cluster size, in the GNFW profile, to θ_{5R500} for the 158 ESZ identified clusters. The figure displays the measured Y_{5R500} values versus the predicted $Y^{L_X}_{5R500}$ values using X-ray luminosities. The squares stand for integrated Compton parameters obtained from the blind detection whereas the diamonds are integrated Compton parameters re-extracted from the *Planck* channel maps for the MCXC-identified clusters. Figure 10, right panel, displays the ratio of blind to predicted Y_{5R500} versus the ratio of estimated cluster size from blind detection to X-ray cluster size derived from X-ray luminosity. This clearly confirms for the 158 identified clusters that an overestimate of cluster size induces an overestimate of the SZ signal. As seen in the Fig. 10 (left panel), the scatter is significantly reduced from about 43% to 34% by imposing a cluster size. Likewise the offset changes from 80% to 14%.

The dispersion in the predicted integrated Compton parameter is affected by the intrinsic dispersion in the L_{500}-M relation used to derive the predicted SZ quantities as shown in Fig. 11. The selection criterion S/N $\geq$ 6 (blue diamonds in the figure) used to construct the ESZ sample indicates that the high S/N clusters are biased towards larger SZ signals, showing that the obtained positive offset in Fig. 10 (left panel) is indeed expected.

As emphasised, a prior on the cluster size helps to break the degeneracy between Y and cluster-size estimates. As a consequence, the better the cluster size estimate, the more reliable the Compton Y parameter estimate. From a selected subsample of 62 ESZ clusters with XMM-Newton archival data (Planck Collaboration 2011d) we have derived accurate estimates of the X-ray sizes, without using the X-ray luminosities, and the Y_{500} were re-evaluated on the *Planck* channel maps, allowing us to tightly constrain the local SZ versus X-ray scaling properties.

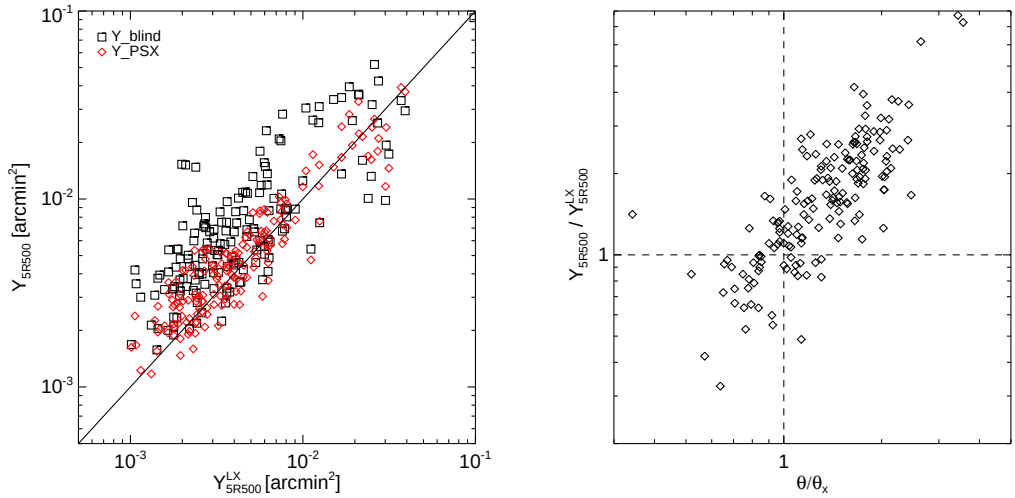

Fig. 10. Left: The scatterplot of the measured integrated Compton parameter Y_{5R500} from the 158 X-ray identified ESZ clusters against the predicted Y^{L_X}. Black squares: Estimated cluster size from blind detections. Red diamonds: Re-computed integrated Compton parameter at X-ray positions and with X-ray derived cluster size. Right: The ratio between the Y values and the predicted Y^{L_X} against the ratio between the estimated cluster size and the predicted size (θ/θ_X).

As shown in Appendix A of Planck Collaboration (2011d), the scatter is reduced even more than in Fig. 10 (left panel) and no offset is observed any more between the predicted and measured Y_{500} values.

6.3. Systematic effects

Due to the cluster size-Y degeneracy discussed above, beam uncertainties are likely to have a significant impact on Y estimates for our candidates because they affect both the original detection and the estimation of cluster size. The beams can be characterised by their shapes and the associated accuracies. The beams for each frequency channel, used for the detection and Y estimate with all methods presented in this study, were assumed Gaussian with FWHM given Planck HFI Core Team (2011b). Uncertainties on the recovered beams have been estimated in Planck HFI Core Team (2011b) and found to range between 1 and 7% (from 100 to 857 GHz). These uncertainties on the beams have been propagated to the Y measurements by applying the MMF3 algorithm on the channel maps varying the beam size within the uncertainties at $\pm1\sigma$. In doing so we treat differently the ESZ clusters with known X-ray cluster size, for which X-ray positions and estimated θ_{5R500} are fixed, and the ESZ clusters or candidate clusters without estimated cluster size for which the Y were re-estimated without prior information. We find that the uncertainty on the obtained Y_{5R500} is of the order of 10% across the ESZ sample.

The *Planck* HFI maps used for the cluster extraction are calibrated to better than 2% for frequencies from 100 to 353 GHz, and to better than 7% beyond [see Planck HFI Core Team (2011b)]. This uncertainty in the calibration is accounted for again by performing the SZ-candidate detection with the MMF3 algorithm on the channel maps. We find that on average, the calibration uncertainty propagates into an uncertainty on the Y less than 2%. The highest *Planck*-HFI frequencies, with the largest calibration uncertainties, have a low impact on the SZ Y measurement and thus do not impact significantly the overall error budget.

Table 3. Systematic error budget on the Y_{5R500} values for the ESZ clusters

Source	Beam	Calibration	Colour correction	Astrophysical contamination
Error contribution	8%	2%	3%	3%

Finally, we have checked that the colour corrections, i.e., the average SZ signal in the HFI bandpasses, induces less than a 3% difference on the estimated Y_{5R500}. The SZ-candidate detection and the Y estimates by the MMF3 algorithm were thus performed without taking into account the integration of the SZ spectrum in the *Planck* bandpasses is negligible.

Table 3 summarises the effects of beam, calibration, and colour correction. It shows that the beam effect is the major source systematic uncertainty in the SZ signal estimate. It is worth noting that the systematic uncertainties are not included in the uncertainties quoted in the ESZ table provided at *http://www.rssd.esa.int/Planck*, (Planck Collaboration 2011g).

6.4. Contamination by astrophysical sources

Galactic and extragalactic sources (both radio and infrared galaxies) are known to lie in the interior of galaxy clusters and hence are a possible source of contamination for the SZ clusters and candidates (Rubiño-Martín & Sunyaev 2003; Aghanim et al. 2005; Lin et al. 2009).

In the course of ESZ validation, we have gone through an inspection of thirteen known clusters which show some poor quality flags. All these clusters were annotated and the notes can be found in Planck Collaboration (2011g). Ten of them are likely to be contaminated by dust emission from our Galaxy or by IR point sources in their vicinity. Two of them were found to be contaminated by NVSS [at 1.4 GHz, Condon et al. (1998)] radio sources that are clearly seen in the LFI channels. Combining data from SUMSS [at 0.85 GHz, Bock et al. (1999)], NVSS, and *Planck*'s LFI and HFI frequencies we find that most radio sources in the ESZ sample have a steep spectrum which

makes their contamination to the SZ signal negligible. Three additional clusters (beyond the thirteen), have relatively bright ($S_{1.4\mathrm{GHz}} > 0.2$ Jy) radio sources in their vicinity ($r < 15$ arcmin). NVSS+LFI data reveal flat spectra (indexes between $\alpha = 0$ and $\alpha = -0.5$). The flux of the radio sources is thus still significant and hence the SZ signal could be affected by their presence.

A statistical analysis has been performed in order to explore the astrophysical contamination over the entire ESZ sample, rather than on an individual cluster basis.

In order to exhibit the initial average level of contamination prior to the use of the MMF algorithm, we have stacked cutouts 4.5 degrees on a side from the channel maps centred at the ESZ cluster/candidate positions from 100 to 857 GHz using a stacking library[17] detailed in Dole et al. (2006) and Bethermin et al. (2010). The Y values per frequency, obtained from aperture photometry on the stacked cutouts, are displayed in red triangles Fig. 12. The spectral signature normalised to the averaged integrated Compton-y over the whole ESZ sample shows quite good agreement with the theoretical SZ spectrum at low frequencies (Fig. 12, black solid line). Above 353 GHz the signal is highly contaminated by IR emission from Galactic dust and IR point sources.

The Y measurements, per frequency, of the MMF3 algorithm normalised to the integrated Compton-y are averaged over the ESZ sample and the resulting spectral energy distribution is compared with the normalised SZ spectrum (see Fig. 12, blue crosses). The excess of emission at high frequencies is significantly reduced by the filtering technique of the MMF algorithm, reinforcing the idea that most of the excess at the highest frequencies is due to large-scale (larger than the beam) fluctuations in Galaxy emission. The remaining excess after the filtering could be due to a combination of small-scale Galactic fluctuations and/or infrared galaxies. In order to quantify the effect of this residual IR emission on the integrated Compton-y determination, an SZ spectrum was fitted to the averaged spectrum. The normalisation was left free. The displayed error bars contain the dispersion of the measured Y per frequency and, added in quadrature, the uncertainties due to the beam, the colour correction, and the calibration ($\sim$ 10%, $\sim$ 3%, $\sim$ 2% respectively). The best value for the normalised integrated Compton parameter is $Y_{\mathrm{fit}} = 1.01$, showing an excellent agreement with the expected spectrum despite the IR excess emission at high frequencies. The same procedure was applied to the 100, 143, 217, and 353 GHz Y values and led to $Y_{\mathrm{fit}_{100-353}} = 0.97$. This shows that, on average, the residual IR contamination has a negligible effect ($\sim$ 3%) on the integrated Compton-y value estimated for the ESZ sample.

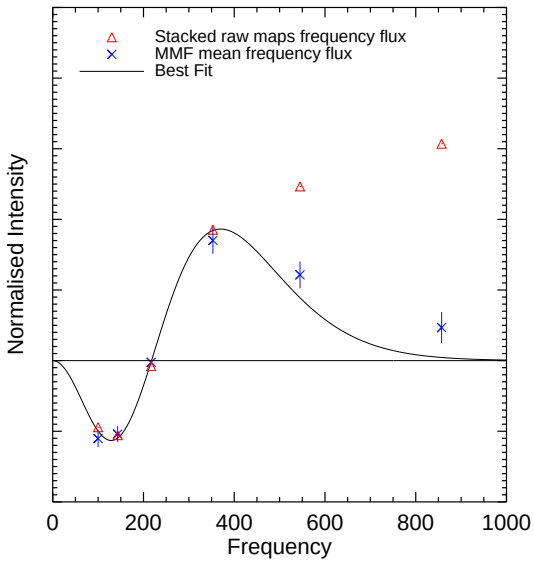

Fig. 12. Average contamination of the ESZ sample by astrophysical sources. Blue crosses: Average Y measurements from MMF3 algorithm normalised to the integrated Compton-y. Red triangles: Y, obtained from aperture photometry on the stacked cutouts in the channel maps prior filtering by the MMF. Black solid line: Normalised theoretical SZ spectrum.

7. Purity and completeness

The ESZ sample is characterised by the fact that a significant fraction of the clusters and candidate clusters lies near a selection cut. In a catalogue of this sort, the properties of the catalogued clusters will not be representative of the true underlying cluster population. For example, if the SZ signal of a cluster is related to a different cluster property such as mass (collectively referred to as 'scaling relations') the observed integrated Compton-y parameter values, Y, will be biased near the selection cut, an effect known as Eddington and Malmquist biases [for discussions in a cluster context see Mantz et al. (2010); Andersson et al. (2010)].

For the full ESZ sample, we do not always have other cluster properties to relate the integrated Compton-y to, but we can nevertheless examine some statistical effects of selection. In order to do this, we generate large mock cluster catalogues whose properties are designed to mimic those of the observed sample. To impose a selection cut on the mock catalogues, we use the *observed* relation between Y_{500} and S/N from the region significantly above the selection cut and extrapolate below it, along with an estimate of scatter again from observations. This is carried out in several redshift bins, and leads to a predicted S/N–Y scaling given by

$$\mathrm{S/N} = 10^{1.38\pm0.03}\,(1+z)^{-5.92\pm0.24}\left[\frac{YE^{-2/3}D_A^2}{10^{-4}\,\mathrm{Mpc}^2}\right],$$

with scatter $\sigma_{\log-\log} = 0.16$ in log-log scale. We then construct large mock catalogues of clusters through drawing of Poisson samples from the Jenkins et al. (2001) mass function normalised with $\sigma_8 = 0.8$, a value consistent with the latest WMAP constraints. To each cluster and consistent with *Planck* observations, we assign values of Y_{5R500} by adopting the Y–M scaling relation from Planck Collaboration (2011d). An S/N value is then assigned as described above, and the cut imposed to create the mock catalogue.

We first use these simulations to estimate the completeness of the ESZ sample as a function of Y_{5R500}. For clusters within a given bin in Y_{5R500}, we extract the fraction of mock clusters which lie above the selection cut. The result is shown in Fig. 13 (solid line), and indicates that the sample becomes significantly incomplete (less than 90% complete) below $Y_{5R500} \simeq 0.013\,\mathrm{arcmin}^2$. This result is fairly insensitive to the assumed mass function normalisation. For example, changing to $\sigma_8 = 0.9$ (dashed line) causes only small variations in the completeness function. For this case, a completeness of 90% is obtained at $Y_{5R500} \simeq 0.010\,\mathrm{arcmin}^2$.

We then analyse the extent to which the mean Y_{5R500} of the observed clusters is biased in relation to the mean Y_{5R500} of the

[17] http://www.ias.u-psud.fr/irgalaxies/ (Bethermin et al. 2010)

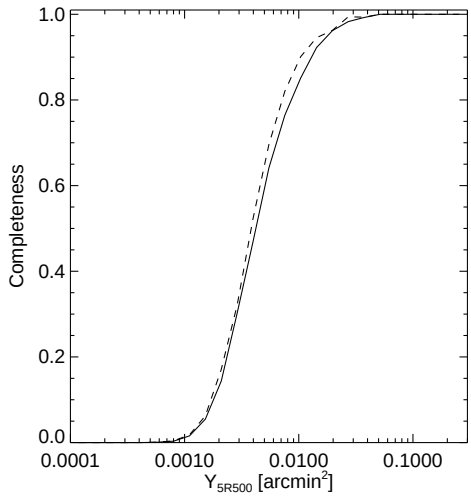

Fig. 13. Expected completeness of the ESZ sample as a function of Y_{5R500}, estimated from mock cluster catalogues.

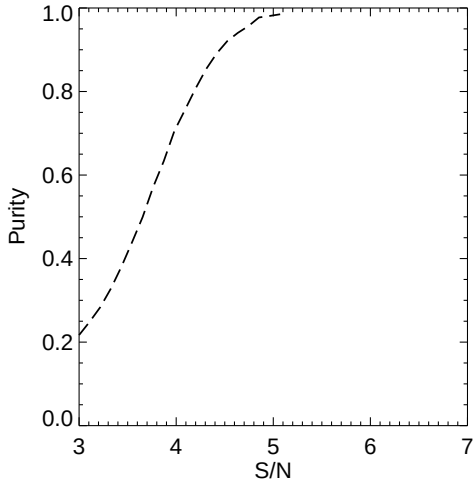

Fig. 15. Purity as a function of S/N from MMF3, based on simulations for the SZ challenge.

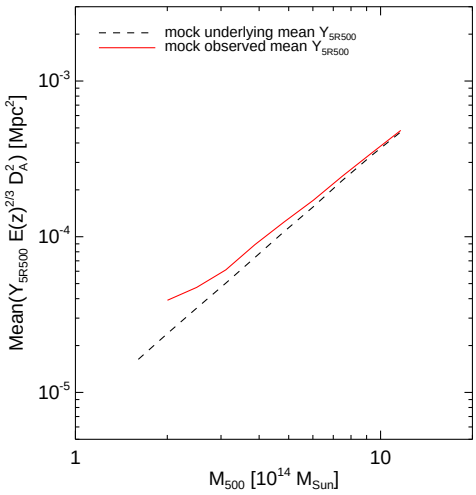

Fig. 14. Expected mean Y_{5R500}, as a function of cluster mass, for the observed sample and for the predicted underlying cluster sample. At low masses, the observed mean rises above the true mean due to Malmquist bias.

underlying cluster distribution, through those clusters with low Y_{5R500} for a given mass being lost via selection. The underlying mean Y_{5R500} in the mock samples is given by the input Y_{500}–M_{500} scaling relation from Planck Collaboration (2011d) and the observed Y_{5R500}–Y_{500} scaling; as shown in Fig. 14 the mean of the observed clusters will be biased upwards from this, the effect becoming significant for $M_{500} < 6 \times 10^{14} \mathrm{M}_{\odot}$. Note that this bias does not imply that the Y_{5R500} measurements for the ESZ clusters are systematically wrong; the bias is because the selection cut prevents those clusters being representative of the true cluster population at those masses.

Finally, numerical simulations based on the *Planck* Sky Model were used to estimate the purity of the *Planck* SZ catalogue. They showed on a simulated sky that a cut in S/N of five ensures 100% purity of the obtained sample (see Fig. 15). However, the simulation does not capture the entire complexity of the real sky and, in particular, the contamination by astrophysical sources emitting above 217 GHz from IR sources and dust emission or cold cores was found to be higher than expected. The final ESZ sample obtained after applying the selection criterion cut in S/N of 6 contained 190 SZ candidates. The validation of the sample showed that one of them was found to be a spurious source identified with dust emission and it was rejected. The remaining candidate new clusters are to be confirmed. The purity of the ESZ sample thus lies between about 95% and 99%.

Although an attempt to characterise the completeness and purity is made, we do not provide a fully characterised selection function along with the ESZ sample. The cluster size-Y degeneracy discussed above, together with the large scatter in the contamination level of the SZ detections due mostly to dust emission, makes it difficult to draw a simple relation between the S/N limit used to construct the sample and the measured Y_{5R500}. It is thus not presently possible to provide a reliable mass limit to our sample. When the telescope beam is larger than the cluster size, a survey is limited by SZ signal. Then, since for the SZ signal the redshift dependence enters through the angular-diameter distance rather than the luminosity distance, the mass selection function is more uniform in SZ than in X-ray surveys. However in our case most of the clusters detected by *Planck* are at nearby redshifts ($z_{\mathrm{median}} = 0.15$) and the majority are resolved, adding even more complexity to the selection function.

8. Statistical characterisation of the ESZ sample

The ESZ sample is the first all-sky sample of high S/N SZ-detected clusters of galaxies produced by *Planck*. Its high reliability is ensured by the high S/N of the reported detections and by the subsequent validation process. The S/N of the objects in the sample, obtained from blind detection using MMF3 on the reference channel maps, are displayed in Fig. 16. They range between 6 and 29 with median S/N of about eight. Six clusters, including A2163 with S/N = 26 and Coma with S/N = 22, are in the tail of the S/N distribution with S/N above 20. The twelve confirmed *Planck* new SZ clusters, included in the ESZ, have their S/N distributed between 6.3 and 11.5. Additional confirmed new clusters with lower S/N are given in Planck Collaboration (2011b). The eight candidate new clusters yet to be confirmed have S/N ranging from 6 to 8.5.

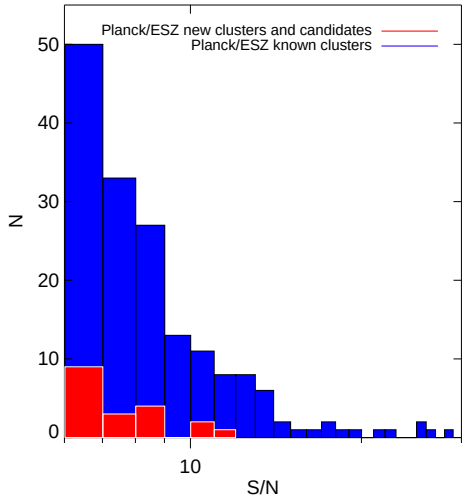

Fig. 16. Distribution of S/N (for the full ESZ sample: clusters and candidate clusters).

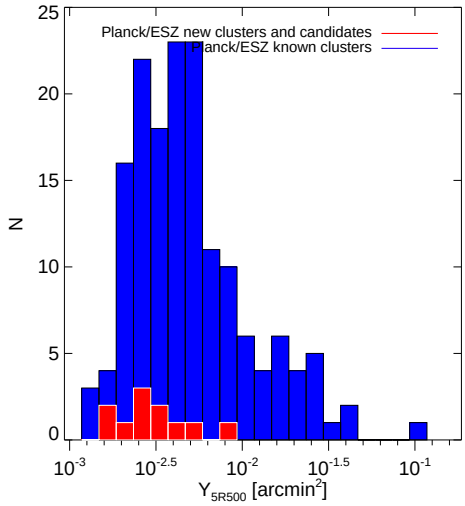

Fig. 17. Distribution of ESZ sample in integrated Compton parameter Y.

The ESZ provides us with measures of the integrated Compton parameter within a $5R500$ sphere, Y_{5R500}, for 189 clusters or candidates. For about 80% of the known clusters in the ESZ, this is the very first SZ measure performed in their direction. The integrated Compton parameter of the whole sample, displayed in Fig. 17, shows that the SZ signal extends over about two orders of magnitude from about 1.5×10^{-3} to 120×10^{-3} arcmin^2. Unsurprisingly, the largest value is that of the Coma cluster. Moreover, the estimated cluster sizes from the MMF3 algorithm for the ESZ clusters and candidates are all above $5\theta_{500} = 8$ arcmin, indicating that the high S/N clusters under study can all be considered as extended sources. We compare the estimated cluster size (from blind detection) with the X-ray cluster size obtained from the X-ray observation of the confirmed SZ clusters, considered as a representative cluster size. We find that the SZ blind size is generally larger than the X-ray cluster size; it can be two times larger. As discussed previously, due to the cluster size-Y degeneracy this affects the integrated Compton parameter measurement.

Using the MCXC compilation and the XMM-Newton observations of the confirmed *Planck* SZ candidates, we obtain masses, M_{500}, estimated from mass proxies (luminosity, L–M relation, or Y_X) for 167 clusters out of the 189 of the ESZ sample. Furthermore, using the redshift information compiled in the MCXC that we retrieved during the validation process and the redshift estimates from XMM-Newton follow-up observations, we gather the redshifts for 173 clusters of the ESZ sample. The distributions of redshifts and masses are exhibited in Figs. 18 and 19, respectively. The redshifts of the ESZ sample are distributed in the range of small to moderate redshifts from about $z = 0.01$ to $z = 0.55$, with a median redshift of 0.15. The vast majority of the ESZ clusters, 86%, are thus nearby ones lying below $z = 0.3$. Most of the newly-discovered clusters confirmed by XMM-Newton within the ESZ sample have redshifts of the order of 0.4. Among the new *Planck* clusters confirmed by XMM-Newton, but with S/N lower than 6, released outside the ESZ we find a cluster with $z = 0.54$. As for the mass distribution of the ESZ clusters, it spans over a decade with cluster masses ranging from 0.9 to $15 \times 10^{14}\ M_\odot$ within a surveyed volume of the order of 3.5×10^{10}Mpc^3. It is worth noting that in surveying the whole sky, *Planck* has a unique capability to detect rare massive clusters in the exponential tail of the mass function. Indeed, among the 21 newly discovered clusters confirmed by XMM-Newton in total (pilot follow-up programme and high-S/N programme) three have total masses of $10 \times 10^{14}\ M_\odot$ or larger and two of them are high S/N clusters in the ESZ sample.

In order to check the consistency of the cosmological model, we compare the measured Y_{5R500} with the X-ray predicted $Y^{L_X}_{5R500}$ that is derived in a given cosmology. To do so, we use the 158 ESZ clusters with X-ray-based size estimates. We vary the cosmological parameter H_0, in a range of 30 to 100 km/s/Mpc assuming a flat universe ($\Omega_m = 0.3$ and $\Omega_\Lambda = 1 - \Omega_m$). The integrated Compton parameters of the 158 clusters were re-estimated from the *Planck* data with the size $5R_{500}$ obtained for each explored set of cosmological parameters. The predicted SZ signals are then compared with the SZ signal measured by *Planck* providing us with the best value for H_0. We find that h is barely constrained, with a best estimate of $H_0 = 71^{+10}_{-20}$ km s^{-1} Mpc^{-1} (1σ uncertainty).

8.1. Comparison with existing catalogues

After the first blind detection of galaxy clusters through their SZ signature by SPT (Staniszewski et al. 2009) and further discoveries by both SPT (Vanderlinde et al. 2010) and ACT (Menanteau et al. 2010), *Planck* with its broad frequency coverage provides the first sample of SZ clusters detected blindly over the whole sky. For its first and early release, *Planck* delivers to the community 189 clusters and candidates with S/N $\geq$ 6 in the ESZ sample, and an additional ten clusters at lower S/N. In total, the 30 new SZ-discovered clusters or candidates by *Planck* double the number of new clusters provided by ACT and SPT during the last year based on their 455 deg^2 and 178 deg^2 respective surveys. Moreover, *Planck* provides the first homogeneous SZ measurements for many known X-ray or optical clusters.

It is worth examining the distribution of the SZ clusters in the M-z plane (see Fig. 20). The range of redshifts covered by the *Planck* ESZ sample, from $z = 0.01$ to 0.55 with more than 80% of the clusters lying below $z = 0.3$, is quite complementary to the high redshift range explored by ACT and SPT experiments, from $z \simeq 0.15$ to 1.2. The comparison of the estimated masses from the different experiments is complicated by the fact

that they are obtained using different approaches, from the use of X-ray proxies to that of mass-significance relations. Overall, we can see from Fig. 20 that the SPT cluster masses quoted in Vanderlinde et al. (2010) range between 1 and $5 \times 10^{14}\,M_{\odot}$. As mentioned previously, *Planck*, being an all-sky survey, spans a broader cluster mass range from 0.9 to $10 \times 10^{14}\,M_{\odot}$ and is particularly adapted to the detection of very massive clusters in the tail of the distribution.

The combination of *Planck* with ACT and SPT experiments already nicely samples the *M*-*z* plane (see Fig. 22). In particular the highest redshift clusters are accessible to ACT and SPT and the most massive clusters to *Planck*. Moreover, *Planck* already samples the low-mass low-redshift space quite well and will provide us with a robust reference point in this range. With the deeper observations of the whole sky, combined with appropriate follow-up programmes for redshift estimates, *Planck* will be able to explore the cluster mass function in its most cosmologically interesting regimes: high redshifts and high masses. However, the detection of the highest redshift clusters is likely to be hampered by the dilution by *Planck* beam. A combination of the *Planck* ACT, and SPT carefully taking into account the selection functions of all three experiments will thus be needed to fully take advantage of SZ clusters as a cosmological probe.

Moreover, combining the data from a sample of clusters with different resolutions (including high-resolution imaging of SZ clusters with interferometric experiments like SZA and CARMA) will allow us to perform detailed studies of extended clusters and have a much better handle on the pressure profile from SZ data directly.

Although the ESZ sample is not a catalogue with a fully characterised selection function, it is worth comparing it to the ROSAT-based cluster catalogues. To do this we take advantage of the MCXC, which contains not only NORAS and REFLEX but other survey-based and serendipitous cluster catalogues. Using the homogenised cluster properties of the MCXC compilation, we can moreover predict the SZ signal and the S/N ratio for a measurement of the Compton *Y* parameter. In order to do this we estimate the *Planck* noise from real noise maps at the cluster positions using MMF3. Using this information, we compared the number of detected clusters in the ESZ at $S/N \geq 6$ to the number predicted at that level of significance. We find very good overall agreement in terms of detected and predicted clusters, despite the fact that the predictions we use are based on X-ray-selected clusters from the MCXC compilation and that the cluster model used for the prediction does not account for the dispersion in the scaling relations, and despite the noise properties of channel maps being inhomogeneous across the sky. Only 26 MCXC clusters with predicted $S/N \geq 6$ are not within the ESZ sample. For 20 of these clusters information on the presence of a cool core or peculiar morphology is available in the literature. We find that 13 of these host cool cores. For these clusters, the X-ray luminosity is boosted due to the central density peak. The mass predicted from the luminosity, and hence the predicted SZ signal, is over-estimated. For 3 clusters the luminosity measurements adopted in the MCXC are not reliable because of evidence of AGN contamination (e.g., A689). The remaining four clusters are peculiar because they have very asymmetric morphologies or are located in superclusters (e.g., A3526 in Centaurus and the A901/A902 system), making the SZ signal predictions highly uncertain.

There is a large overlap between the *Planck* ESZ sample and the RASS-based cluster catalogues, in particular REFLEX and NORAS (Fig. 21). The 162 SZ candidates identified with X-ray clusters from the MCXC compilation are predominantly clusters from the REFLEX (74) and NORAS (59) surveys, which corresponds to an overlap of 17% and 13% with the REFLEX and NORAS surveys respectively. The eleven ESZ clusters confirmed by XMM-Newton with $S/N \geq 6$ were found to lie just around the REFLEX flux limit (only two are above this limit).

It is thus interesting to compare the ESZ sample mass and redshift distributions with those of the RASS-based catalogues. This is illustrated in Figs. 18 and 19 in which the RASS-based mass and redshift distribution divided by ten are over-plotted on the ESZ histograms in thick solid line. We find that the ESZ clusters with masses below $4 \times 10^{14}\,M_{\odot}$ represent only 12% of the RASS-based clusters in the same mass range; however

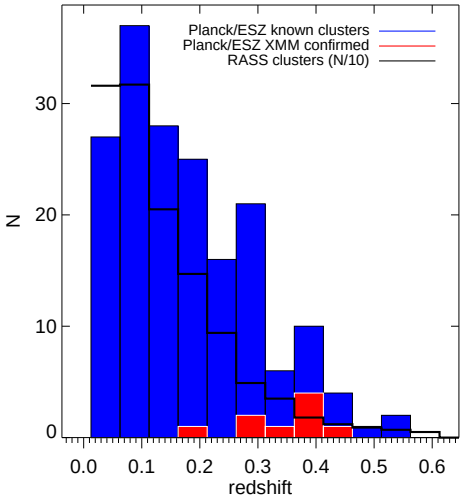

Fig. 18. Distribution of ESZ sample in redshift. The 177 identified ESZ clusters with redshift (from optical or X-ray observations) are in blue, the ESZ clusters confirmed with XMM-Newton in red, and the RASS clusters (number density divided by 10) in black solid line.

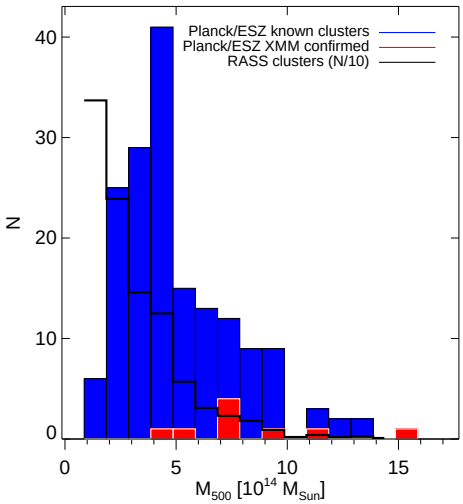

Fig. 19. Distribution of ESZ sample in mass. The 167 identified ESZ clusters with masses are in blue, the ESZ clusters confirmed with XMM-Newton in red, and the RASS clusters (number density divided by 10) in black solid line.

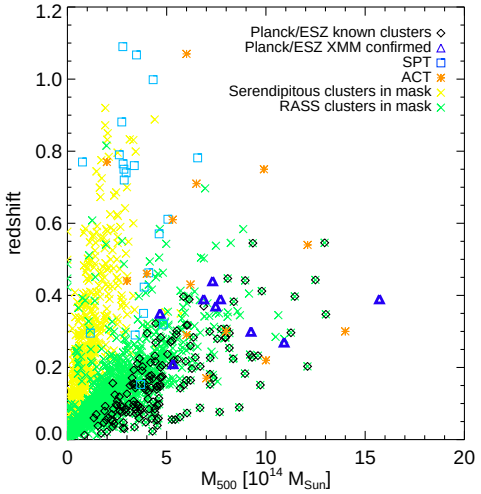

Fig. 20. The 158 clusters from the *Planck* ESZ sample identified with known X-ray clusters in redshift–mass space, compared with SPT and ACT samples from Menanteau et al. (2010); Vanderlinde et al. (2010), as well as serendipitous and RASS clusters.

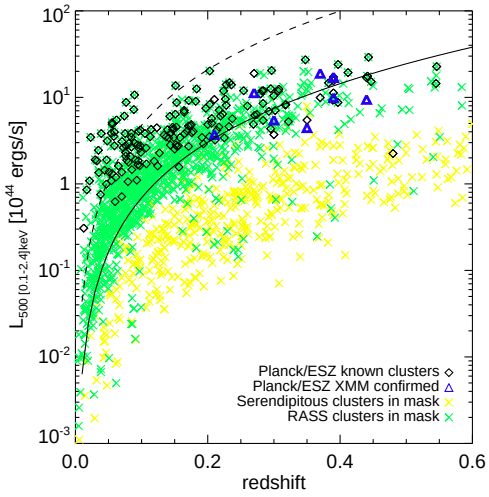

Fig. 21. The 158 clusters from the *Planck* ESZ sample identified with known X-ray clusters in redshift–luminosity space, compared with serendipitous and RASS clusters.

they represent 90% of the RASS-based clusters at higher masses $M \geq 9{\times}10^{14}\,M_{\odot}$. As for the redshift distribution, the *Planck* ESZ clusters represent 14% of the RASS-based clusters with redshifts lower than 0.3 and they constitute 31% of the RASS-based clusters above $z = 0.3$.

The SDSS-MaxBCG cluster catalogue is the basis of the study of optical-SZ scaling relations (Planck Collaboration 2011e) in *Planck* data. It is used in particular to measure an integrated Compton parameter, $Y_{5R500}^{\mathrm{MaxBCG}}$, from the *Planck* channel maps at the MaxBCG position using fixed cluster size according to published weak-lensing calibrated mass–richness relations for the MaxBCG catalogue. Only 20 clusters from the MaxBCG have a measured S/N larger than six and are thus expected to

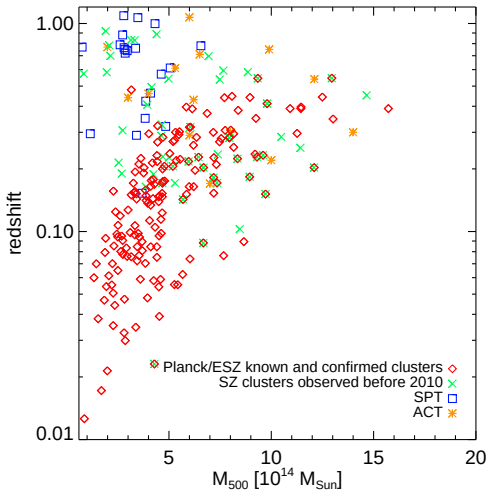

Fig. 22. The ESZ sample compared to the previously observed SZ clusters in redshift–mass space.

be within the ESZ selection[18]. Among them, 18 are effectively associated with ESZ clusters (within a search radius of five arcminutes). One of the two clusters not in the ESZ sample is Abell 1246 ($z = 0.18$). The second is a fortuitous association with a low-redshift ($z = 0.06$) group of the MaxBCG catalogue near the position of Abell 1795, which is detected in the ESZ catalogue.

9. Summary

Thanks to its all-sky coverage and to its frequency range spanning the SZ decrement and increment, *Planck* provides us with the very first all-sky S/N-selected SZ sample. This early release sample of high-reliability SZ clusters and candidates (S/N from 6 to 29) was constructed using a matched multi-filter detection technique. It was validated using *Planck*-internal quality assessment, external X-ray and optical data, and a multi-frequency follow-up programme for confirmation relying mostly on XMM-Newton snapshot observations. The ESZ sample comprises 189 candidates, of which 20 are candidate new clusters and 169 have X-ray or optical counterparts. Of these, 162 were observed in X-ray. *Planck* provides for the first time SZ observations for about 80% of the ESZ clusters and hence a homogeneously measured SZ signal. Twelve candidate clusters in total, out of the 20, have been confirmed. One candidate was confirmed by AMI and WISE. Eleven were confirmed with XMM-Newton, including two candidates found to be double clusters on the sky.

The clusters in the ESZ sample are mostly at moderate redshifts lying between $z = 0.01$ and $z = 0.55$, with 86% of them below $z = 0.3$. The ESZ-cluster masses span over a decade from 0.9 to $15 \times 10^{14}\,M_{\odot}$, i.e. up to the highest masses. The ESZ, constructed using clear selection criteria, is a nearly complete (90% above $E^{-2/3}(z)Y_{5R500}D_A^2 \simeq 4 \times 10^{-4}\,\mathrm{Mpc}^2$), high-purity (above 95%) SZ cluster sample. However, as mentioned above, it is not possible at the present stage to provide users with a full selection function.

Thanks to its all-sky coverage, *Planck* has a unique capability to detect the rarest and most massive clusters in the exponential tail of the mass function. Planck is detecting new clusters

[18] This number accounts for the possible association of a candidate new cluster with a cluster from Wen et al. (2009).

in a region of the mass-redshift plane that is sparsely populated by the RASS catalogues. As a matter of fact, two of the newly-discovered clusters in the ESZ and confirmed by XMM-Newton have estimated total masses larger than $10^{15}\,M_{\odot}$. Furthermore, as indicated by XMM-Newton snapshot observations, most of the new clusters have low luminosity and a disturbed morphology, suggestive of a complex dynamical state. *Planck* may thus have started to reveal a non-negligible population of massive dynamically-perturbed objects that is under-represented in X-ray surveys.

A significant fraction of the ESZ clusters have good archival X-ray and optical data. In addition, the ESZ sample should motivate follow-up effort by the community. It will hence serve as a valuable reference for studies of cluster physics at low and moderate redshifts (e.g., galaxy properties versus intra-cluster gas physics, metallicities, dynamical state and its evolution, etc). These studies will require multi-wavelength observations including further SZ observations at higher spatial resolution and observations in X-rays (with XMM-Newton, Chandra, and Suzaku), in the optical (imaging and spectroscopy), and in the radio (e.g., with LOFAR).

The ensemble of early results on the SZ signal in *Planck* using a selected local sub-sample of ESZ clusters with high-quality XMM-Newton archival data (Planck Collaboration 2011d) and using the compilation of about 1600 MCXC clusters (Planck Collaboration 2011c), shows excellent agreement between observed SZ quantities and X-ray-based predictions underlining the robustness and consistency of our overall view of ICM properties. These results shed light on long-standing questions regarding the consistency between the SZ and X-ray view of hot gas in galaxy clusters. In contrast, the SZ signal-to-optical-richness relation measured from the SDSS-MaxBCG cluster catalogue Planck Collaboration (2011e) has a lower SZ signal than predicted. Extensive SZ-optical statistical studies of this kind are new. The result, and the origin of the difference, may be related to the cluster population, such as the existence of a sub-population of X-ray under-luminous clusters, or to selection effects in optical cluster catalogues.

In the future, *Planck* will deliver a larger all-sky SZ cluster catalogue. The characterisation of the *Planck* selection function together with the construction of this legacy catalogue, including its validation using follow up observations in particular with XMM-Newton, will be one of the major activities.

The usefulness of the SZ cluster abundance in achieving precise cosmological constraints relies on several theoretical and observational requirements. One of them is the ability to obtain redshift measurements for each confirmed SZ cluster. Cross-correlation of *Planck* data with the only available large optical survey to date, the Sloan Digital Sky Survey (SDSS), can be used to confirm *Planck* candidates and provide redshift estimates on a area restricted to the SDSS coverage area. The XMM-Newton confirmation observations can provide redshift estimates, but only for the X-ray brightest clusters. A significant follow-up effort in the optical (with ESO, ENO, and NOAO facilities) has thus been put in place by the *Planck* collaboration in order to obtain redshifts (photometric and spectroscopic) for the SZ clusters. Another key requirement for the cosmological use of the SZ catalogue is the derivation of the fundamental relation between the integrated Compton parameter, Y, and the cluster mass and its evolution with redshift. Planck Collaboration (2011d) have calibrated the local relation between Y and Y_X, the analogue of the SZ signal, measured from the X-ray gas mass and temperature, to an unprecedented precision and, for the first time, have demonstrated its remarkably small intrinsic scatter. We will build an even more robust and controlled observational proxy of the cluster mass which is fundamental for cosmological applications. To do this, specific studies based on the comparison of mass estimates from lensing, X-rays and SZ observations for a selected representative sample of the SZ catalogue will be most crucial.

Finally, combining *Planck* all-sky SZ data with near future and planned observations of the large-scale structure by large surveys, e.g., PANSTARRS, LOFAR, Euclid, LSST, and e-ROSITA, will allow us to understand the physical processes governing large-scale structure formation and evolution.

Acknowledgements. The authors thank N. Schartel, ESA XMM-Newton project scientist, for granting the Director Discretionary Time used for confirmation of SZ Planck candidates. This research has made use of the following databases: SIMBAD, operated at CDS, Strasbourg, France; the NED database, which is operated by the Jet Propulsion Laboratory, California Institute of Technology, under contract with the National Aeronautics and Space Administration; BAX, operated by the Laboratoire d'Astrophysique de Tarbes-Toulouse (LATT), under contract with the Centre National d'Etudes Spatiales (CNES), SZ repository operated by IAS Data and Operation Center (IDOC) under contract with CNES. The authors acknowledge the use of software provided by the US National Virtual Observatory. A description of the Planck Collaboration and a list of its members, indicating which technical or scientific activities they have been involved in, can be found at http://www.rssd.esa.int/Planck.

References

Abell, G. O. 1958, ApJS, 3, 211
Aghanim, N., de Luca, A., Bouchet, F. R., Gispert, R., & Puget, J. L. 1997, A&A, 325, 9
Aghanim, N., Hansen, S. H., & Lagache, G. 2005, A&A, 439, 901
Aghanim, N., Majumdar, S., & Silk, J. 2008, Reports on Progress in Physics, 71, 066902
Ameglio, S., Borgani, S., Diaferio, A., & Dolag, K. 2006, MNRAS, 369, 1459
Andersson, K., Benson, B. A., Ade, P. A. R., et al. 2010, ArXiv e-prints, arXiv:1006.3068
Appenzeller, I., Thiering, I., Zickgraf, F., et al. 1998, ApJS, 117, 319
Arnaud, M., Pointecouteau, E., & Pratt, G. W. 2007, A&A, 474, L37
Arnaud, M., Pratt, G. W., Piffaretti, R., et al. 2010, A&A, 517, A92
Battistelli, E. S., De Petris, M., Lamagna, L., et al. 2002, ApJ, 580, L101
Battistelli, E. S., De Petris, M., Lamagna, L., et al. 2006, ApJ, 645, 826
Benson, B. A., Church, S. E., Ade, P. A. R., et al. 2003, ApJ, 592, 674
Bethermin, M., Dole, H., Beelen, A., & Aussel, H. 2010, VizieR Online Data Catalog, 351, 29078
Birkinshaw, M. 1999, Phys. Rep., 310, 97
Birkinshaw, M. & Gull, S. F. 1978, Nature, 274, 111
Birkinshaw, M. & Hughes, J. P. 1994, ApJ, 420, 33
Birkinshaw, M. & Lancaster, K. 2005, in Background Microwave Radiation and Intracluster Cosmology, ed. F. Melchiorri & Y. Rephaeli, 127–+
Bock, D., Large, M. I., & Sadler, E. M. 1999, AJ, 117, 1578
Böhringer, H., Schuecker, P., Pratt, G. W., et al. 2007, A&A, 469, 363
Bonamente, M., Joy, M. K., LaRoque, S. J., et al. 2006, ApJ, 647, 25
Borgani, S. 2006, ArXiv Astrophysics e-prints astro-ph/0605575,
Borgani, S., Murante, G., Springel, V., et al. 2004, MNRAS, 348, 1078
Budavári, T., Dobos, L., Szalay, A. S., et al. 2007, in Astronomical Society of the Pacific Conference Series, Vol. 376, Astronomical Data Analysis Software and Systems XVI, ed. R. A. Shaw, F. Hill, & D. J. Bell, 559–+
Carlstrom, J. E., Ade, P. A. R., Aird, K. A., et al. 2009, ArXiv e-prints, arXiv:0907.4445
Carlstrom, J. E., Holder, G. P., & Reese, E. D. 2002, ARA&A, 40, 643
Carvalho, P., Rocha, G., & Hobson, M. P. 2009, MNRAS, 393, 681
Cavaliere, A. & Fusco-Femiano, R. 1978, A&A, 70, 677
Colafrancesco, S., Marchegiani, P., & Palladino, E. 2003, A&A, 397, 27
Condon, J. J., Cotton, W. D., Greisen, E. W., et al. 1998, AJ, 115, 1693
Cortese, L., Gavazzi, G., Boselli, A., Iglesias-Paramo, J., & Carrasco, L. 2004, A&A, 425, 429
da Silva, A. C., Barbosa, D., Liddle, A. R., & Thomas, P. A. 2001, MNRAS, 326, 155
da Silva, A. C., Kay, S. T., Liddle, A. R., & Thomas, P. A. 2004, MNRAS, 348, 1401
Dawson, K. S., Holzapfel, W. L., Carlstrom, J. E., et al. 2001, ApJ, 553, L1
De Petris, M., Mainella, G., Nerozzi, A., et al. 1999, New A Rev., 43, 297
Dobbs, M., Halverson, N. W., Ade, P. A. R., et al. 2006, New A Rev., 50, 960

Dole, H., Lagache, G., Puget, J., et al. 2006, A&A, 451, 417
Douspis, M., Aghanim, N., Evrard, L., & Langer, M. 2011, in preparation
Douspis, M., Aghanim, N., & Langer, M. 2006, A&A, 456, 819
Einasto, M., Einasto, J., Tago, E., Müller, V., & Andernach, H. 2001, AJ, 122, 2222
Fixsen, D. J., Cheng, E. S., Cottingham, D. A., et al. 1994, ApJ, 420, 457
Génova-Santos, R., Rubiño-Martín, J. A., Rebolo, R., et al. 2005, MNRAS, 363, 79
Ghizzardi, S., Rossetti, M., & Molendi, S. 2010, A&A, 516, A32+
Glenn, J., Bock, J. J., Chattopadhyay, G., et al. 1998, in Presented at the Society of Photo-Optical Instrumentation Engineers (SPIE) Conference, Vol. 3357, Society of Photo-Optical Instrumentation Engineers (SPIE) Conference Series, ed. T. G. Phillips, 326–334
Gómez, P. L., Romer, K. A., Peterson, J., et al. 2003, in Astronomical Society of the Pacific Conference Series, Vol. 301, Astronomical Society of the Pacific Conference Series, ed. S. Bowyer & C.-Y. Hwang, 495–+
Górski, K. M., Hivon, E., Banday, A. J., et al. 2005, ApJ, 622, 759
Grego, L., Carlstrom, J. E., Reese, E. D., et al. 2001, ApJ, 552, 2
Haiman, Z., Mohr, J. J., & Holder, G. P. 2001, ApJ, 553, 545
Herranz, D., Sanz, J. L., Hobson, M. P., et al. 2002, MNRAS, 336, 1057
Hinshaw, G., Weiland, J. L., Hill, R. S., et al. 2009, ApJS, 180, 225
Holzapfel, W. L., Wilbanks, T. M., Ade, P. A. R., et al. 1997, ApJ, 479, 17
Horellou, C., Nord, M., Johansson, D., & Lévy, A. 2005, A&A, 441, 435
Hurier, G., Hildebrandt, S. R., & Macias-Perez, J. F. 2010, ArXiv e-prints, arXiv:1007.1149
Hurley-Walker, T. A. C. N., Brown, M. L., Davies, M. L., et al. 2011, ArXiv e-prints, arXiv:1103.0947
Itoh, N., Kohyama, Y., & Nozawa, S. 1998, ApJ, 502, 7
Jenkins, A., Frenk, C. S., White, S. D. M., et al. 2001, MNRAS, 321, 372
Jones, M., Saunders, R., Alexander, P., et al. 1993, Nature, 365, 320
Kashlinsky, A., Atrio-Barandela, F., Kocevski, D., & Ebeling, H. 2008, ApJ, 686, L49
Kobayashi, S., Sasaki, S., & Suto, Y. 1996, PASJ, 48, L107
Koester, B. P., McKay, T. A., Annis, J., et al. 2007, ApJ, 660, 239
Komatsu, E., Kitayama, T., Suto, Y., et al. 1999, ApJ, 516, L1
Kravtsov, A. V., Vikhlinin, A., & Nagai, D. 2006, ApJ, 650, 128
Lamarre, J., Puget, J., Ade, P. A. R., et al. 2010, A&A, 520, A9+
Lamarre, J. M., Giard, M., Pointecouteau, E., et al. 1998, ApJ, 507, L5
Lancaster, K., Genova-Santos, R., Falcòn, N., et al. 2005, MNRAS, 359, 16
Levine, E. S., Schulz, A. E., & White, M. 2002, ApJ, 577, 569
Lin, Y., Partridge, B., Pober, J. C., et al. 2009, ApJ, 694, 992
Luzzi, G., Shimon, M., Lamagna, L., et al. 2009, ApJ, 705, 1122
Majumdar, S. & Mohr, J. J. 2004, ApJ, 613, 41
Mantz, A., Allen, S. W., Ebeling, H., Rapetti, D., & Drlica-Wagner, A. 2010, MNRAS, 406, 1773
Marriage, T. A., Acquaviva, V., Ade, P. A. R., et al. 2010, ArXiv e-prints, arXiv:1010.1065
Melin, J., Bartlett, J. G., & Delabrouille, J. 2006, A&A, 459, 341
Melin, J.-B., Aghanim, N., Bartelmann, M., et al. 2011
Menanteau, F., González, J., Juin, J., et al. 2010, ApJ, 723, 1523
Miville-Deschênes, M. & Lagache, G. 2005, ApJS, 157, 302
Montier, L. A., Pelkonen, V., Juvela, M., Ristorcelli, I., & Marshall, D. J. 2010, A&A, 522, A83+
Motl, P. M., Hallman, E. J., Burns, J. O., & Norman, M. L. 2005, ApJ, 623, L63
Muchovej, S., Mroczkowski, T., Carlstrom, J. E., et al. 2007, ApJ, 663, 708
Nagai, D., Kravtsov, A. V., & Vikhlinin, A. 2007, ApJ, 668, 1
Pfrommer, C., Enßlin, T. A., Springel, V., Jubelgas, M., & Dolag, K. 2007, MNRAS, 378, 385
Piffaretti, R., Arnaud, M., Pratt, G. W., Pointecouteau, E., & Melin, J. 2010, arXiv e-print, arXiv:1007.1916
Piffaretti, R. & Valdarnini, R. 2008, A&A, 491, 71
Plagge, T., Benson, B. A., Ade, P. A. R., et al. 2010, ApJ, 716, 1118
Planck Collaboration. 2011a, Planck early results 07: The Early Release Compact Source Catalogue (Submitted to A&A, [arXiv:astro-ph/1101.2041])
Planck Collaboration. 2011b, Planck early results 09: XMM-Newton follow-up for validation of Planck cluster candidates (Submitted to A&A, [arXiv:astro-ph/1101.2025])
Planck Collaboration. 2011c, Planck early results 10: Statistical analysis of Sunyaev-Zeldovich scaling relations for X-ray galaxy clusters (Submitted to A&A, [arXiv:astro-ph/1101.2043])
Planck Collaboration. 2011d, Planck early results 11: Calibration of the local galaxy cluster Sunyaev-Zeldovich scaling relations (Submitted to A&A, [arXiv:astro-ph/1101.2026])
Planck Collaboration. 2011e, Planck early results 12: Cluster Sunyaev-Zeldovich optical Scaling relations (Submitted to A&A, [arXiv:astro-ph/1101.2027])
Planck Collaboration. 2011f, Planck early results 23: The Galactic cold core population revealed by the first all-sky survey (Submitted to A&A, [arXiv:astro-ph/1101.2035])
Planck Collaboration. 2011g, The Explanatory Supplement to the Planck Early Release Compact Source Catalogue (ESA)
Planck HFI Core Team. 2011a, Planck early results 04: First assessment of the High Frequency Instrument in-flight performance (Submitted to A&A, [arXiv:astro-ph/1101.2039])
Planck HFI Core Team. 2011b, Planck early results 06: The High Frequency Instrument data processing (Submitted to A&A, [arXiv:astro-ph/1101.2048])
Pointecouteau, E., Giard, M., & Barret, D. 1998, A&A, 336, 44
Pointecouteau, E., Giard, M., Benoit, A., et al. 1999, ApJ, 519, L115
Pratt, G. W., Croston, J. H., Arnaud, M., & Böhringer, H. 2009, A&A, 498, 361
Reese, E. D., Carlstrom, J. E., Joy, M., et al. 2002, ApJ, 581, 53
Rephaeli, Y. 1995, ARA&A, 33, 541
Rubiño-Martín, J. A. & Sunyaev, R. A. 2003, MNRAS, 344, 1155
Sadat, R., Blanchard, A., Kneib, J., et al. 2004, A&A, 424, 1097
Schneider, D. P., Bahcall, J. N., Gunn, J. E., & Dressler, A. 1992, AJ, 103, 1047
Shimon, M. & Rephaeli, Y. 2004, New A, 9, 69
Silk, J. & White, S. D. M. 1978, ApJ, 226, L103
Staniszewski, Z., Ade, P. A. R., Aird, K. A., et al. 2009, ApJ, 701, 32
Story, K., Aird, K. A., Andersson, K., et al. 2011, ArXiv e-prints, arXiv:1102.2189
Sunyaev, R. A. & Zeldovich, I. B. 1980, ARA&A, 18, 537
Sunyaev, R. A. & Zeldovich, Y. B. 1972, Comments on Astrophysics and Space Physics, 4, 173
Udomprasert, P. S., Mason, B. S., Readhead, A. C. S., & Pearson, T. J. 2004, ApJ, 615, 63
Uzan, J., Aghanim, N., & Mellier, Y. 2004, Phys. Rev. D, 70, 083533
Vanderlinde, K., Crawford, T. M., de Haan, T., et al. 2010, ApJ, 722, 1180
Vikhlinin, A., Burenin, R. A., Ebeling, H., et al. 2009, ApJ, 692, 1033
Weller, J., Battye, R. A., & Kneissl, R. 2002, Physical Review Letters, 88, 231301
Wen, Z. L., Han, J. L., & Liu, F. S. 2009, ApJS, 183, 197
Williamson, R., Benson, B. A., High, F. W., et al. 2011, ArXiv e-prints, arXiv:1101.1290
Wright, E. L., Eisenhardt, P. R. M., Mainzer, A. K., et al. 2010, AJ, 140, 1868
Wu, J., Chiueh, T., Huang, C., et al. 2008, Modern Physics Letters A, 23, 1675
Zemcov, M., Borys, C., Halpern, M., Mauskopf, P., & Scott, D. 2007, MNRAS, 376, 1073
Zemcov, M., Rex, M., Rawle, T. D., et al. 2010, A&A, 518, L16+
Zwart, J. T. L., Barker, R. W., Biddulph, P., et al. 2008, MNRAS, 391, 1545
Zwicky, F., Herzog, E., & Wild, P. 1961, Catalogue of galaxies and of clusters of galaxies, Vol. I, ed. Zwicky, F., Herzog, E., & Wild, P.

Appendix A: ESZ sample extract

Table A.3 is an extract from the *Planck* ESZ sample available at *www.rssd.esa.int/Planck* aiming at presenting the content of the released product. Four entries are given as examples for each category (*Planck* ESZ known clusters, *Planck* ESZ new confirmed clusters, *Planck* ESZ clusters candidates). In the present extract, only Galactic longitudes and latitudes are given. The ESZ sample contains, in addition, the right ascensions and declinations for all the entries.

For each entry the following fields are provided:

- Name: *Planck* Name of Cluster Candidate
- GLON: Galactic Longitude from *Planck*
- GLAT: Galactic latitude from *Planck*
- S/N: Signal-to-noise ratio returned by the matched multi-Filter algorithm (MMF3)
- ID: External Identifier of *Planck* Clusters e.g. Coma, Abell 2163 etc
- z: Redshift of Cluster from the MCXC X-ray cluster compilation unless otherwise stated in the individual notes
- Θ_X: Angular size at $5R500$ from X-ray data
- Y_{PSX}: Integrated Compton parameter at X-ray position and within $5R500$ (Θ_X) in arcmin^2,
- Y_{PSX}^{ERR}: Uncertainty in Integrated Compton parameter at X-ray position and within $5R500$ (Θ_X) in arcmin^2
- Θ: Estimated angular size from matched multi-Filter (MMF3),

– Y: Integrated Compton parameter at *Planck* position and within Θ, from matched multi-Filter (MMF3) in arcmin^2
– Y^{ERR}: Uncertainty in Integrated Compton parameter at *Planck* position and within Θ from matched multi-Filter (MMF3) in arcmin^2

[1] Aalto University Metsähovi Radio Observatory, Metsähovintie 114, FIN-02540 Kylmälä, Finland
[2] Agenzia Spaziale Italiana Science Data Center, c/o ESRIN, via Galileo Galilei, Frascati, Italy
[3] Astroparticule et Cosmologie, CNRS (UMR7164), Université Denis Diderot Paris 7, Bâtiment Condorcet, 10 rue A. Domon et Léonie Duquet, Paris, France
[4] Astrophysics Group, Cavendish Laboratory, University of Cambridge, J J Thomson Avenue, Cambridge CB3 0HE, U.K.
[5] Atacama Large Millimeter/submillimeter Array, ALMA Santiago Central Offices, Alonso de Cordova 3107, Vitacura, Casilla 763 0355, Santiago, Chile
[6] CITA, University of Toronto, 60 St. George St., Toronto, ON M5S 3H8, Canada
[7] CNRS, IRAP, 9 Av. colonel Roche, BP 44346, F-31028 Toulouse cedex 4, France
[8] California Institute of Technology, Pasadena, California, U.S.A.
[9] Centre of Mathematics for Applications, University of Oslo, Blindern, Oslo, Norway
[10] Centro de Astrofísica, Universidade do Porto, Rua das Estrelas, 4150-762 Porto, Portugal
[11] DAMTP, University of Cambridge, Centre for Mathematical Sciences, Wilberforce Road, Cambridge CB3 0WA, U.K.
[12] DSM/Irfu/SPP, CEA-Saclay, F-91191 Gif-sur-Yvette Cedex, France
[13] DTU Space, National Space Institute, Juliane Mariesvej 30, Copenhagen, Denmark
[14] Departamento de Física, Universidad de Oviedo, Avda. Calvo Sotelo s/n, Oviedo, Spain
[15] Department of Astronomy and Astrophysics, University of Toronto, 50 Saint George Street, Toronto, Ontario, Canada
[16] Department of Physics & Astronomy, University of British Columbia, 6224 Agricultural Road, Vancouver, British Columbia, Canada
[17] Department of Physics and Astronomy, University of Southern California, Los Angeles, California, U.S.A.
[18] Department of Physics and Astronomy, University of Sussex, Brighton BN1 9QH, U.K.
[19] Department of Physics, Gustaf Hällströmin katu 2a, University of Helsinki, Helsinki, Finland
[20] Department of Physics, Princeton University, Princeton, New Jersey, U.S.A.
[21] Department of Physics, Purdue University, 525 Northwestern Avenue, West Lafayette, Indiana, U.S.A.
[22] Department of Physics, University of California, Berkeley, California, U.S.A.
[23] Department of Physics, University of California, One Shields Avenue, Davis, California, U.S.A.
[24] Department of Physics, University of California, Santa Barbara, California, U.S.A.
[25] Department of Physics, University of Illinois at Urbana-Champaign, 1110 West Green Street, Urbana, Illinois, U.S.A.
[26] Dipartimento di Fisica G. Galilei, Università degli Studi di Padova, via Marzolo 8, 35131 Padova, Italy
[27] Dipartimento di Fisica, Università La Sapienza, P. le A. Moro 2, Roma, Italy
[28] Dipartimento di Fisica, Università degli Studi di Milano, Via Celoria, 16, Milano, Italy
[29] Dipartimento di Fisica, Università degli Studi di Trieste, via A. Valerio 2, Trieste, Italy
[30] Dipartimento di Fisica, Università di Ferrara, Via Saragat 1, 44122 Ferrara, Italy
[31] Dipartimento di Fisica, Università di Roma Tor Vergata, Via della Ricerca Scientifica, 1, Roma, Italy
[32] Discovery Center, Niels Bohr Institute, Blegdamsvej 17, Copenhagen, Denmark
[33] Dpto. Astrofísica, Universidad de La Laguna (ULL), E-38206 La Laguna, Tenerife, Spain
[34] European Southern Observatory, ESO Vitacura, Alonso de Cordova 3107, Vitacura, Casilla 19001, Santiago, Chile
[35] European Space Agency, ESAC, Camino bajo del Castillo, s/n, Urbanización Villafranca del Castillo, Villanueva de la Cañada, Madrid, Spain
[36] European Space Agency, ESAC, Planck Science Office, Camino bajo del Castillo, s/n, Urbanización Villafranca del Castillo, Villanueva de la Cañada, Madrid, Spain
[37] European Space Agency, ESTEC, Keplerlaan 1, 2201 AZ Noordwijk, The Netherlands
[38] GEPI, Observatoire de Paris, Section de Meudon, 5 Place J. Janssen, 92195 Meudon Cedex, France
[39] Helsinki Institute of Physics, Gustaf Hällströmin katu 2, University of Helsinki, Helsinki, Finland
[40] INAF - Osservatorio Astronomico di Padova, Vicolo dell'Osservatorio 5, Padova, Italy
[41] INAF - Osservatorio Astronomico di Roma, via di Frascati 33, Monte Porzio Catone, Italy
[42] INAF - Osservatorio Astronomico di Trieste, Via G.B. Tiepolo 11, Trieste, Italy
[43] INAF/IASF Bologna, Via Gobetti 101, Bologna, Italy
[44] INAF/IASF Milano, Via E. Bassini 15, Milano, Italy
[45] INRIA, Laboratoire de Recherche en Informatique, Université Paris-Sud 11, Bâtiment 490, 91405 Orsay Cedex, France
[46] IPAG: Institut de Planétologie et d'Astrophysique de Grenoble, Université Joseph Fourier, Grenoble 1 / CNRS-INSU, UMR 5274, Grenoble, F-38041, France
[47] Imperial College London, Astrophysics group, Blackett Laboratory, Prince Consort Road, London, SW7 2AZ, U.K.
[48] Infrared Processing and Analysis Center, California Institute of Technology, Pasadena, CA 91125, U.S.A.
[49] Institut Néel, CNRS, Université Joseph Fourier Grenoble I, 25 rue des Martyrs, Grenoble, France
[50] Institut d'Astrophysique Spatiale, CNRS (UMR8617) Université Paris-Sud 11, Bâtiment 121, Orsay, France
[51] Institut d'Astrophysique de Paris, CNRS UMR7095, Université Pierre & Marie Curie, 98 bis boulevard Arago, Paris, France
[52] Institut de Ciències de l'Espai, CSIC/IEEC, Facultat de Ciències, Campus UAB, Torre C5 par-2, Bellaterra 08193, Spain
[53] Institute of Astronomy and Astrophysics, Academia Sinica, Taipei, Taiwan
[54] Institute of Astronomy, University of Cambridge, Madingley Road, Cambridge CB3 0HA, U.K.
[55] Institute of Theoretical Astrophysics, University of Oslo, Blindern, Oslo, Norway
[56] Instituto de Astrofísica de Canarias, C/Vía Láctea s/n, La Laguna, Tenerife, Spain
[57] Instituto de Física de Cantabria (CSIC-Universidad de Cantabria), Avda. de los Castros s/n, Santander, Spain
[58] Jet Propulsion Laboratory, California Institute of Technology, 4800 Oak Grove Drive, Pasadena, California, U.S.A.
[59] Jodrell Bank Centre for Astrophysics, Alan Turing Building, School of Physics and Astronomy, The University of Manchester, Oxford Road, Manchester, M13 9PL, U.K.
[60] Kavli Institute for Cosmology Cambridge, Madingley Road, Cambridge, CB3 0HA, U.K.
[61] LERMA, CNRS, Observatoire de Paris, 61 Avenue de l'Observatoire, Paris, France
[62] Laboratoire AIM, IRFU/Service d'Astrophysique - CEA/DSM - CNRS - Université Paris Diderot, Bât. 709, CEA-Saclay, F-91191 Gif-sur-Yvette Cedex, France
[63] Laboratoire Traitement et Communication de l'Information, CNRS (UMR 5141) and Télécom ParisTech, 46 rue Barrault F-75634 Paris Cedex 13, France

[64] Laboratoire de Physique Subatomique et de Cosmologie, CNRS/IN2P3, Université Joseph Fourier Grenoble I, Institut National Polytechnique de Grenoble, 53 rue des Martyrs, 38026 Grenoble cedex, France
[65] Laboratoire de l'Accélérateur Linéaire, Université Paris-Sud 11, CNRS/IN2P3, Orsay, France
[66] Lawrence Berkeley National Laboratory, Berkeley, California, U.S.A.
[67] MPA Partner Group, Key Laboratory for Research in Galaxies and Cosmology, Shanghai Astronomical Observatory, Chinese Academy of Sciences, Nandan Road 80, Shanghai 200030, China
[68] Max-Planck-Institut für Astrophysik, Karl-Schwarzschild-Str. 1, 85741 Garching, Germany
[69] Max-Planck-Institut für Extraterrestrische Physik, Giessenbachstraße, 85748 Garching, Germany
[70] MilliLab, VTT Technical Research Centre of Finland, Tietotie 3, Espoo, Finland
[71] National University of Ireland, Department of Experimental Physics, Maynooth, Co. Kildare, Ireland
[72] Niels Bohr Institute, Blegdamsvej 17, Copenhagen, Denmark
[73] Observational Cosmology, Mail Stop 367-17, California Institute of Technology, Pasadena, CA, 91125, U.S.A.
[74] Optical Science Laboratory, University College London, Gower Street, London, U.K.
[75] SISSA, Astrophysics Sector, via Bonomea 265, 34136, Trieste, Italy
[76] SUPA, Institute for Astronomy, University of Edinburgh, Royal Observatory, Blackford Hill, Edinburgh EH9 3HJ, U.K.
[77] School of Physics and Astronomy, Cardiff University, Queens Buildings, The Parade, Cardiff, CF24 3AA, U.K.
[78] Space Research Institute (IKI), Russian Academy of Sciences, Profsoyuznaya Str, 84/32, Moscow, 117997, Russia
[79] Space Sciences Laboratory, University of California, Berkeley, California, U.S.A.
[80] Stanford University, Dept of Physics, Varian Physics Bldg, 382 Via Pueblo Mall, Stanford, California, U.S.A.
[81] Tartu Observatory, Toravere, Tartumaa, 61602, Estonia
[82] Tuorla Observatory, Department of Physics and Astronomy, University of Turku, Väisäläntie 20, FIN-21500, Piikkiö, Finland
[83] Universität Heidelberg, Institut für Theoretische Astrophysik, Albert-Überle-Str. 2, 69120, Heidelberg, Germany
[84] Université Denis Diderot (Paris 7), 75205 Paris Cedex 13, France
[85] Université de Toulouse, UPS-OMP, IRAP, F-31028 Toulouse cedex 4, France
[86] Universities Space Research Association, Stratospheric Observatory for Infrared Astronomy, MS 211-3, Moffett Field, CA 94035, U.S.A.
[87] University Observatory, Ludwig Maximilian University of Munich, Scheinerstrasse 1, 81679 Munich, Germany
[88] University of Granada, Departamento de Física Teórica y del Cosmos, Facultad de Ciencias, Granada, Spain
[89] University of Miami, Knight Physics Building, 1320 Campo Sano Dr., Coral Gables, Florida, U.S.A.
[90] Warsaw University Observatory, Aleje Ujazdowskie 4, 00-478 Warszawa, Poland

Table A.1. ESZ sample.

Name	GLON	GLAT	S/N	ID	z	Θ_X	Y_{PSX}	Y_{PSX}^{ERR}	Θ	Y	Y^{ERR}
PLCKG111.0+31.7	110.98	31.73	28.93	A2256	0.06	83.14	0.0242	0.0009	NaN	NaN	NaN
PLCKG57.3+88.0	57.34	88.01	21.94	Coma	0.02	203.37	0.1173	0.0054	NaN	NaN	NaN
PLCKG239.3+24.8	239.28	24.77	25.67	A0754	0.05	90.56	0.0330	0.0012	NaN	NaN	NaN
PLCKG272.1-40.2	272.11	-40.15	25.90	A3266	0.06	84.19	0.0282	0.0012	NaN	NaN	NaN
PLCKG6.8+30.5	6.78	30.47	26.40	A2163	0.20	37.81	0.0173	0.0007	NaN	NaN	NaN
PLCKG340.9-33.3	340.89	-33.35	22.02	A3667	0.06	93.11	0.0266	0.0014	NaN	NaN	NaN
PLCKG266.0-21.3	266.04	-21.25	19.75	1ES 0657-55.8	0.30	26.96	0.0067	0.0003	NaN	NaN	NaN
PLCKG44.2+48.7	44.23	48.68	18.46	A2142	0.09	70.33	0.0241	0.0013	NaN	NaN	NaN
PLCKG93.9+34.9	93.92	34.91	17.31	A2255	0.08	58.11	0.0103	0.0006	NaN	NaN	NaN
PLCKG164.2-38.9	164.19	-38.89	13.79	A0401	0.07	74.42	0.0193	0.0016	NaN	NaN	NaN
PLCKG72.6+41.5	72.63	41.46	17.44	A2219	0.23	31.40	0.0085	0.0005	NaN	NaN	NaN
PLCKG263.7-22.5	263.67	-22.54	16.70	A3404	0.16	35.89	0.0064	0.0004	NaN	NaN	NaN
PLCKG97.7+38.1	97.74	38.12	14.65	A2218	0.17	31.96	0.0044	0.0003	NaN	NaN	NaN
PLCKG263.2-25.2	263.21	-25.21	11.24	A3395	0.05	76.98	0.0073	0.0009	NaN	NaN	NaN
PLCKG262.3-35.4	262.25	-35.37	15.19	ACO S0520	0.30	24.30	0.0034	0.0003	NaN	NaN	NaN
PLCKG74.0-27.8	73.97	-27.82	14.25	A2390	0.23	31.17	0.0056	0.0005	NaN	NaN	NaN
PLCKG332.2-46.4	332.23	-46.37	13.89	A3827	0.10	52.41	0.0086	0.0007	NaN	NaN	NaN
PLCKG265.0-48.9	265.01	-48.95	13.95	A3158	0.06	77.52	0.0117	0.0010	NaN	NaN	NaN
PLCKG115.2-72.1	115.16	-72.09	13.14	A0085	0.06	94.22	0.0210	0.0018	NaN	NaN	NaN
PLCKG316.3+28.5	316.35	28.54	12.85	A3571	0.04	124.14	0.0372	0.0031	NaN	NaN	NaN
PLCKG86.5+15.3	86.46	15.30	12.33	CIZA J1938.3+5409	0.26	24.59	0.0031	0.0003	NaN	NaN	NaN
PLCKG33.8+77.2	33.78	77.16	12.39	A1795	0.06	85.79	0.0169	0.0014	NaN	NaN	NaN
PLCKG6.5+50.5	6.48	50.55	13.36	A2029	0.08	77.99	0.0180	0.0015	NaN	NaN	NaN
PLCKG349.5-59.9	349.46	-59.95	13.93	ACO S1063	0.35	24.94	0.0046	0.0003	NaN	NaN	NaN
PLCKG186.4+37.3	186.39	37.26	12.61	A0697	0.28	25.00	0.0051	0.0005	NaN	NaN	NaN
PLCKG229.9+15.3	229.94	15.30	12.46	A0644	0.07	67.06	0.0116	0.0010	NaN	NaN	NaN
PLCKG149.7+34.7	149.73	34.70	11.57	A0665	0.18	34.94	0.0060	0.0005	NaN	NaN	NaN
PLCKG3.9-59.4	3.91	-59.42	12.06	A3888	0.15	38.39	0.0061	0.0005	NaN	NaN	NaN
PLCKG312.0+30.7	312.00	30.72	9.04	A3558	0.05	97.34	0.0223	0.0024	NaN	NaN	NaN
PLCKG313.9-17.1	313.87	-17.11	11.57	CIZA J1601.7-7544	0.15	40.63	0.0078	0.0007	NaN	NaN	NaN
PLCKG335.6-46.5	335.59	-46.46	10.17	A3822	0.08	57.18	0.0084	0.0008	NaN	NaN	NaN
PLCKG288.6-37.7	288.62	-37.66	9.86	A3186	0.13	35.86	0.0053	0.0006	NaN	NaN	NaN
PLCKG315.7-18.0	315.71	-18.04	11.44	A3628	0.10	48.10	0.0088	0.0008	NaN	NaN	NaN
PLCKG263.2-23.4	263.16	-23.41	10.08	ACO S0592	0.23	28.97	0.0032	0.0003	NaN	NaN	NaN
PLCKG149.2+54.2	149.24	54.19	11.58	A1132	0.14	36.78	0.0052	0.0005	NaN	NaN	NaN
PLCKG21.1+33.3	21.09	33.26	10.61	A2204	0.15	45.35	0.0076	0.0007	NaN	NaN	NaN
PLCKG322.0-48.0	321.96	-47.98	11.27	A3921	0.09	49.92	0.0053	0.0006	NaN	NaN	NaN
PLCKG182.4-28.3	182.44	-28.30	12.77	A0478	0.09	65.31	0.0167	0.0014	NaN	NaN	NaN
PLCKG242.0+14.9	241.97	14.86	10.49	A3411	0.17	31.37	0.0041	0.0005	NaN	NaN	NaN
PLCKG29.0+44.6	29.01	44.56	10.25	A2147	0.04	108.90	0.0148	0.0021	NaN	NaN	NaN
PLCKG228.5+53.1	228.50	53.13	12.20	Zw 3179	0.14	33.59	0.0022	0.0005	NaN	NaN	NaN
PLCKG62.9+43.7	62.93	43.71	10.03	A2199	0.03	138.17	0.0241	0.0023	NaN	NaN	NaN
PLCKG206.0-39.5	205.96	-39.48	9.26	MACS J0417.5-1154	0.44	20.43	0.0038	0.0004	NaN	NaN	NaN
PLCKG336.6-55.4	336.59	-55.45	10.29	A3911	0.10	47.65	0.0057	0.0006	NaN	NaN	NaN
PLCKG67.2+67.5	67.23	67.46	11.03	A1914	0.17	37.08	0.0057	0.0005	NaN	NaN	NaN
PLCKG92.7+73.5	92.73	73.46	11.26	A1763	0.23	27.79	0.0045	0.0004	NaN	NaN	NaN
PLCKG146.3-15.6	146.33	-15.59	7.10	CIZA J0254.4+4134	0.02	199.50	0.0392	0.0060	NaN	NaN	NaN
PLCKG112.5+57.0	112.46	57.04	9.81	A1767	0.07	56.20	0.0053	0.0006	NaN	NaN	NaN
PLCKG55.6+31.9	55.60	31.86	9.27	A2261	0.22	30.74	0.0049	0.0005	NaN	NaN	NaN
PLCKG58.3+18.6	58.28	18.59	9.19	CIZA J1825.3+3026	0.06	62.65	0.0087	0.0009	NaN	NaN	NaN
PLCKG159.9-73.5	159.86	-73.47	10.63	A0209	0.21	28.17	0.0053	0.0005	NaN	NaN	NaN
PLCKG282.5+65.2	282.49	65.17	8.49	ZwCl 1215.1+0400	0.08	60.24	0.0095	0.0012	NaN	NaN	NaN
PLCKG313.4+61.1	313.36	61.12	10.12	A1689	0.18	37.34	0.0071	0.0008	NaN	NaN	NaN
PLCKG53.5+59.5	53.52	59.54	8.50	A2034	0.11	44.04	0.0055	0.0008	NaN	NaN	NaN
PLCKG244.3-32.1	244.34	-32.14	8.39	RBS0653	0.28	24.88	0.0029	0.0004	NaN	NaN	NaN
PLCKG46.9+56.5	46.88	56.50	9.07	A2069	0.11	45.41	0.0067	0.0008	NaN	NaN	NaN
PLCKG294.7-37.0	294.67	-37.03	8.64	RXCJ0303.7-7752	0.27	22.29	0.0028	0.0004	NaN	NaN	NaN
PLCKG346.6+35.0	346.60	35.05	9.38	RXCJ1514.9-1523	0.22	26.97	0.0048	0.0006	NaN	NaN	NaN
PLCKG243.6+67.8	243.57	67.76	8.57	A1307	0.08	52.20	0.0062	0.0007	NaN	NaN	NaN
PLCKG166.1+43.4	166.13	43.39	9.23	A0773	0.22	28.20	0.0038	0.0004	NaN	NaN	NaN
PLCKG226.2+76.8	226.25	76.77	9.18	A1413	0.14	39.97	0.0058	0.0006	NaN	NaN	NaN
PLCKG107.1+65.3	107.11	65.31	8.85	A1758A	0.28	24.73	0.0031	0.0004	NaN	NaN	NaN
PLCKG42.8+56.6	42.83	56.62	8.36	A2065	0.07	63.04	0.0099	0.0011	NaN	NaN	NaN
PLCKG125.6-64.1	125.59	-64.14	10.47	A0119	0.04	88.65	0.0141	0.0017	NaN	NaN	NaN
PLCKG57.3-45.4	57.27	-45.36	8.11	MACS J2211.7-0349	0.40	21.56	0.0032	0.0004	NaN	NaN	NaN
PLCKG33.5-48.4	33.46	-48.43	9.24	A2384A	0.09	44.21	0.0054	0.0006	NaN	NaN	NaN

Table A.2. The ESZ sample (continued)

Name	GLON	GLAT	S/N	ID	z	Θ_X	Y_{PSX}	Y_{PSX}^{ERR}	Θ	Y	Y^{ERR}
PLCKG241.8-24.0	241.78	-24.00	8.94	A3378	0.14	37.79	0.0038	0.0005	NaN	NaN	NaN
PLCKG46.5-49.4	46.50	-49.44	8.55	A2420	0.08	54.47	0.0064	0.0008	NaN	NaN	NaN
PLCKG304.9+45.5	304.90	45.45	8.99	A1644	0.05	88.28	0.0152	0.0018	NaN	NaN	NaN
PLCKG209.6-36.5	209.56	-36.49	7.96	A0496	0.03	126.18	0.0162	0.0021	NaN	NaN	NaN
PLCKG57.0-55.1	56.97	-55.08	8.16	MACS J2243.3-0935	0.45	17.55	0.0029	0.0004	NaN	NaN	NaN
PLCKG56.8+36.3	56.81	36.32	9.15	A2244	0.10	53.36	0.0058	0.0007	NaN	NaN	NaN
PLCKG57.6+34.9	57.61	34.94	9.54	A2249	0.08	52.39	0.0052	0.0007	NaN	NaN	NaN
PLCKG49.2+30.9	49.20	30.86	8.33	RXC J1720.1+2637	0.16	36.32	0.0043	0.0005	NaN	NaN	NaN
PLCKG6.7-35.5	6.70	-35.54	8.45	A3695	0.09	52.90	0.0059	0.0008	NaN	NaN	NaN
PLCKG77.9-26.6	77.91	-26.65	8.36	A2409	0.15	36.46	0.0040	0.0005	NaN	NaN	NaN
PLCKG8.9-81.2	8.94	-81.24	8.39	A2744	0.31	23.17	0.0042	0.0005	NaN	NaN	NaN
PLCKG106.7-83.2	106.73	-83.23	8.55	A2813	0.29	21.45	0.0036	0.0004	NaN	NaN	NaN
PLCKG269.5+26.4	269.52	26.42	8.40	A1060	0.01	216.51	0.0215	0.0029	NaN	NaN	NaN
PLCKG180.2+21.0	180.24	21.05	8.36	MACS J0717.5+3745	0.55	17.74	0.0028	0.0004	NaN	NaN	NaN
PLCKG241.7-30.9	241.74	-30.89	7.42	RXCJ0532.9-3701	0.27	22.43	0.0028	0.0004	NaN	NaN	NaN
PLCKG332.9-19.3	332.89	-19.28	7.72	CIZA J1813.3-6127	0.15	35.99	0.0043	0.0006	NaN	NaN	NaN
PLCKG48.1+57.2	48.05	57.18	7.14	A2061	0.08	54.65	0.0067	0.0010	NaN	NaN	NaN
PLCKG139.2+56.4	139.20	56.36	7.65	A1351	0.32	18.52	0.0012	0.0003	NaN	NaN	NaN
PLCKG306.7+61.1	306.68	61.06	8.02	A1650	0.08	57.80	0.0095	0.0012	NaN	NaN	NaN
PLCKG167.7+17.6	167.66	17.65	8.11	ZwCl 0634.1+4750	0.17	31.51	0.0045	0.0005	NaN	NaN	NaN
PLCKG49.3+44.4	49.34	44.38	7.40	A2175	0.10	42.77	0.0054	0.0009	NaN	NaN	NaN
PLCKG226.2-21.9	226.18	-21.91	7.28	A0550	0.10	45.53	0.0047	0.0007	NaN	NaN	NaN
PLCKG195.8-24.3	195.77	-24.31	7.23	A0520	0.20	31.04	0.0046	0.0006	NaN	NaN	NaN
PLCKG253.5-33.7	253.48	-33.72	6.73	A3343	0.19	26.95	0.0022	0.0004	NaN	NaN	NaN
PLCKG250.9-36.3	250.91	-36.26	8.62	A3322	0.20	27.92	0.0028	0.0004	NaN	NaN	NaN
PLCKG256.5-65.7	256.45	-65.71	7.77	A3016	0.22	26.97	0.0029	0.0004	NaN	NaN	NaN
PLCKG324.5-45.0	324.50	-44.97	6.22	RBS1847	0.10	44.97	0.0039	0.0005	NaN	NaN	NaN
PLCKG113.8+44.4	113.82	44.35	7.80	A1895	0.22	23.20	0.0012	0.0002	NaN	NaN	NaN
PLCKG125.7+53.9	125.71	53.86	7.36	A1576	0.30	20.94	0.0019	0.0003	NaN	NaN	NaN
PLCKG266.8+25.1	266.84	25.08	8.19	A3444	0.25	27.46	0.0027	0.0004	NaN	NaN	NaN
PLCKG216.6+47.0	216.62	47.02	7.48	RXC J0949.8+1707	0.38	19.99	0.0021	0.0004	NaN	NaN	NaN
PLCKG228.2+75.2	228.16	75.19	7.13	MACS J1149.5+2223	0.55	15.93	0.0016	0.0003	NaN	NaN	NaN
PLCKG342.3-34.9	342.32	-34.91	7.24	RXCJ2023.4-5535	0.23	24.13	0.0029	0.0004	NaN	NaN	NaN
PLCKG342.8-30.5	342.82	-30.46	6.01	A3651	0.06	54.80	0.0044	0.0009	NaN	NaN	NaN
PLCKG124.2-36.5	124.22	-36.49	7.74	A0115	0.20	31.15	0.0050	0.0007	NaN	NaN	NaN
PLCKG257.3-22.2	257.34	-22.18	7.13	A3399	0.20	25.71	0.0019	0.0003	NaN	NaN	NaN
PLCKG118.4+39.3	118.45	39.34	6.33	RXCJ1354.6+7715	0.40	17.24	0.0016	0.0003	NaN	NaN	NaN
PLCKG118.6+28.6	118.60	28.56	6.41	A2294	0.18	29.83	0.0022	0.0004	NaN	NaN	NaN
PLCKG229.6+78.0	229.64	77.96	7.45	A1443	0.27	21.40	0.0027	0.0004	NaN	NaN	NaN
PLCKG180.6+76.7	180.62	76.65	7.48	A1423	0.21	25.40	0.0027	0.0004	NaN	NaN	NaN
PLCKG2.7-56.2	2.75	-56.18	6.48	A3856	0.14	35.56	0.0031	0.0005	NaN	NaN	NaN
PLCKG347.2-27.4	347.19	-27.35	8.19	ACO S0821	0.24	24.78	0.0022	0.0004	NaN	NaN	NaN
PLCKG71.6+29.8	71.61	29.80	7.47	Zw 8284	0.16	27.18	0.0024	0.0004	NaN	NaN	NaN
PLCKG36.7+14.9	36.72	14.92	6.98	RXCJ1804.4+1002	0.15	35.28	0.0035	0.0006	NaN	NaN	NaN
PLCKG18.5-25.7	18.53	-25.72	7.30	RXCJ2003.5-2323	0.32	20.71	0.0027	0.0004	NaN	NaN	NaN
PLCKG237.0-26.7	236.96	-26.67	7.03	A3364	0.15	35.80	0.0030	0.0005	NaN	NaN	NaN
PLCKG273.6+63.3	273.64	63.28	7.30	A1437	0.13	37.96	0.0051	0.0007	NaN	NaN	NaN
PLCKG46.1+27.2	46.08	27.18	7.34	MACS J1731.6+2252	0.39	17.79	0.0021	0.0003	NaN	NaN	NaN
PLCKG49.7-49.5	49.67	-49.51	6.88	A2426	0.10	47.77	0.0038	0.0007	NaN	NaN	NaN
PLCKG143.2+65.2	143.25	65.22	7.34	A1430	0.21	24.27	0.0023	0.0003	NaN	NaN	NaN
PLCKG296.4-32.5	296.41	-32.49	7.20	ACO S0405	0.06	62.06	0.0044	0.0007	NaN	NaN	NaN
PLCKG269.3-49.9	269.31	-49.88	6.51	A3126	0.09	47.30	0.0040	0.0007	NaN	NaN	NaN
PLCKG83.3-31.0	83.29	-31.03	6.19	RXC J2228.6+2036	0.41	19.89	0.0021	0.0004	NaN	NaN	NaN
PLCKG304.7-31.7	304.67	-31.67	6.37	A4023	0.19	25.68	0.0020	0.0004	NaN	NaN	NaN
PLCKG39.9-40.0	39.86	-39.99	6.32	A2345	0.18	29.89	0.0031	0.0005	NaN	NaN	NaN
PLCKG56.0-34.9	55.98	-34.89	7.03	A2355	0.12	33.85	0.0036	0.0005	NaN	NaN	NaN
PLCKG303.8+33.7	303.76	33.66	6.05	A3528S	0.05	68.17	0.0085	0.0014	NaN	NaN	NaN
PLCKG163.7+53.5	163.72	53.53	7.46	A0980	0.16	32.07	0.0030	0.0004	NaN	NaN	NaN
PLCKG318.1-29.6	318.13	-29.58	6.63	RXCJ1947.3-7623	0.22	25.55	0.0031	0.0005	NaN	NaN	NaN
PLCKG244.7+32.5	244.70	32.49	6.27	A0868	0.15	31.25	0.0029	0.0005	NaN	NaN	NaN
PLCKG284.5+52.4	284.46	52.44	7.27	RXCJ1206.2-0848	0.44	18.33	0.0029	0.0004	NaN	NaN	NaN
PLCKG260.0-63.4	260.03	-63.44	7.29	RXCJ0232.2-4420	0.28	23.09	0.0024	0.0004	NaN	NaN	NaN
PLCKG253.0-56.1	252.97	-56.05	6.79	A3112	0.08	65.98	0.0047	0.0007	NaN	NaN	NaN
PLCKG234.6+73.0	234.59	73.02	6.39	A1367	0.02	169.59	0.0146	0.0029	NaN	NaN	NaN
PLCKG278.6+39.2	278.61	39.17	7.57	A1300	0.31	23.38	0.0035	0.0005	NaN	NaN	NaN
PLCKG246.5-26.1	246.52	-26.06	6.52	A3376	0.05	77.30	0.0053	0.0010	NaN	NaN	NaN
PLCKG114.3+64.9	114.34	64.87	6.18	A1703	0.28	20.89	0.0020	0.0003	NaN	NaN	NaN

Table A.3. The ESZ sample (continued)

Name	GLON	GLAT	S/N	ID	z	Θ_X	Y_{PSX}	Y^{ERR}_{PSX}	Θ	Y	Y^{ERR}
PLCKG80.4-33.2	80.38	-33.20	6.06	A2443	0.11	39.40	0.0039	0.0006	NaN	NaN	NaN
PLCKG249.9-39.9	249.88	-39.87	6.25	A3292	0.15	31.40	0.0018	0.0004	NaN	NaN	NaN
PLCKG182.6+55.8	182.64	55.82	6.81	A0963	0.21	27.40	0.0019	0.0004	NaN	NaN	NaN
PLCKG62.4-46.4	62.42	-46.41	6.33	A2440	0.09	47.33	0.0041	0.0007	NaN	NaN	NaN
PLCKG8.4-56.4	8.45	-56.36	6.39	A3854	0.15	33.94	0.0024	0.0005	NaN	NaN	NaN
PLCKG229.2-17.2	229.22	-17.25	6.18	RXCJ0616.3-2156	0.17	28.31	0.0031	0.0005	NaN	NaN	NaN
PLCKG341.0+35.1	340.96	35.12	6.61	ACO S0780	0.24	30.43	0.0030	0.0007	NaN	NaN	NaN
PLCKG218.9+35.5	218.86	35.51	6.87	A0750	0.18	31.52	0.0027	0.0005	NaN	NaN	NaN
PLCKG165.1+54.1	165.09	54.12	6.34	A0990	0.14	35.91	0.0027	0.0005	NaN	NaN	NaN
PLCKG161.4+26.2	161.44	26.23	6.63	A0576	0.04	88.79	0.0076	0.0012	NaN	NaN	NaN
PLCKG295.3+23.3	295.33	23.34	6.11	RXCJ1215.4-3900	0.12	36.31	0.0042	0.0008	NaN	NaN	NaN
PLCKG280.2+47.8	280.20	47.82	7.06	A1391	0.16	30.98	0.0042	0.0006	NaN	NaN	NaN
PLCKG0.4-41.8	0.44	-41.84	6.55	A3739	0.17	31.54	0.0025	0.0005	NaN	NaN	NaN
PLCKG195.6+44.1	195.62	44.05	6.88	A0781	0.30	19.18	0.0017	0.0003	NaN	NaN	NaN
PLCKG241.9+51.5	241.86	51.53	6.96	A1066	0.07	48.70	0.0024	0.0007	NaN	NaN	NaN
PLCKG81.0-50.9	81.00	-50.91	6.76	A2552	0.30	22.98	0.0026	0.0005	NaN	NaN	NaN
PLCKG304.5+32.4	304.50	32.44	6.86	A3532	0.06	69.91	0.0068	0.0015	NaN	NaN	NaN
PLCKG306.8+58.6	306.80	58.61	6.81	A1651	0.08	59.16	0.0077	0.0012	NaN	NaN	NaN
PLCKG172.9+65.3	172.89	65.32	6.30	A1190	0.08	47.15	0.0030	0.0006	NaN	NaN	NaN
PLCKG99.0+24.9	98.95	24.86	6.49	A2312	0.09	41.02	0.0022	0.0004	NaN	NaN	NaN
PLCKG247.2-23.3	247.17	-23.33	6.19	ACO S0579	0.15	31.86	0.0019	0.0004	NaN	NaN	NaN
PLCKG176.3-35.1	176.28	-35.05	6.38	2A0335+096	0.03	126.35	0.0117	0.0025	NaN	NaN	NaN
PLCKG57.9+27.6	57.93	27.64	6.13	ZwCl 1742.1+3306	0.08	58.65	0.0037	0.0008	NaN	NaN	NaN
PLCKG275.2+43.9	275.22	43.92	6.29	A1285	0.11	43.45	0.0044	0.0008	NaN	NaN	NaN
PLCKG96.9+52.5	96.85	52.47	6.12	A1995	0.32	20.73	0.0015	0.0003	NaN	NaN	NaN
PLCKG72.8-18.7	72.80	-18.72	10.10	ZwCl2120.1+2256	0.14	NaN	NaN	NaN	37.22	0.0052	0.0010
PLCKG239.3-26.0	239.29	-26.00	8.64	MACS J0553.4-3342	0.41	NaN	NaN	NaN	17.22	0.0026	0.0006
PLCKG8.3-64.8	8.30	-64.76	8.47	AC114Northern	0.31	NaN	NaN	NaN	43.83	0.0048	0.0010
PLCKG94.0+27.4	94.02	27.43	6.92	H1821+643	0.30	NaN	NaN	NaN	40.25	0.0030	0.0014
PLCKG157.4+30.3	157.43	30.34	6.18	RXJ0748.7+5941	NaN	NaN	NaN	NaN	22.43	0.0025	0.0014
PLCKG345.4-39.3	345.41	-39.34	7.10	ABELL3716S	0.04	NaN	NaN	NaN	118.59	0.0109	0.0032
PLCKG53.4-36.3	53.44	-36.27	6.88	MACS J2135.2-0102	0.32	NaN	NaN	NaN	8.07	0.0018	0.0003
PLCKG271.5-56.6	271.50	-56.56	6.71	ACO S0295	0.30	NaN	NaN	NaN	20.26	0.0025	0.0007
PLCKG86.0+26.7	86.00	26.71	6.55	A2302	0.18	NaN	NaN	NaN	56.62	0.0043	0.0019
PLCKG96.9+24.2	96.88	24.22	6.24	ZwCl1856.8+6616	NaN	NaN	NaN	NaN	20.64	0.0015	0.0005
PLCKG164.6+46.4	164.61	46.39	6.06	ZwCl0934.8+5216	NaN	NaN	NaN	NaN	16.50	0.0018	0.0006
PLCKG285.0-23.7	284.99	-23.71	11.48	null	0.44	19.50	0.0023	0.0002	NaN	NaN	NaN
PLCKG287.0+32.9	286.99	32.92	10.62	null	0.39	25.33	0.0061	0.0006	NaN	NaN	NaN
PLCKG171.9-40.7	171.95	-40.66	10.61	null	0.39	29.56	0.0062	0.0006	NaN	NaN	NaN
PLCKG271.2-31.0	271.20	-30.97	8.48	null	0.27	20.06	0.0020	0.0002	NaN	NaN	NaN
PLCKG262.7-40.9	262.71	-40.91	8.27	ACT-CLJ0438-5419	0.37	18.71	0.0021	0.0002	NaN	NaN	NaN
PLCKG308.3-20.2	308.32	-20.23	8.26	null	0.39	NaN	NaN	NaN	32.81	0.0049	0.0013
PLCKG277.8-51.7	277.75	-51.73	7.40	null	0.21	17.51	0.0027	0.0003	NaN	NaN	NaN
PLCKG286.6-31.3	286.59	-31.25	6.89	null	0.30	28.12	0.0026	0.0004	NaN	NaN	NaN
PLCKG292.5+22.0	292.52	21.99	6.88	null	0.35	25.66	0.0037	0.0006	NaN	NaN	NaN
PLCKG337.1-26.0	337.09	-25.97	6.59	null	0.48	NaN	NaN	NaN	31.56	0.0034	0.0008
PLCKG285.6-17.2	285.64	-17.25	6.35	null	0.12	17.68	0.0016	0.0003	NaN	NaN	NaN
PLCKG225.9-20.0	225.93	-20.00	8.07	null	NaN	NaN	NaN	NaN	28.21	0.0040	0.0011
PLCKG255.6-46.2	255.63	-46.17	8.46	null	NaN	NaN	NaN	NaN	31.23	0.0026	0.0006
PLCKG304.8-41.4	304.84	-41.42	7.58	null	NaN	NaN	NaN	NaN	21.68	0.0022	0.0006
PLCKG121.1+57.0	121.12	57.01	6.66	null	NaN	NaN	NaN	NaN	17.99	0.0016	0.0004
PLCKG283.2-22.9	283.16	-22.93	6.03	null	NaN	NaN	NaN	NaN	26.73	0.0018	0.0008
PLCKG139.6+24.2	139.60	24.19	7.21	null	NaN	NaN	NaN	NaN	24.52	0.0032	0.0013
PLCKG189.8-37.2	189.85	-37.24	6.71	null	NaN	NaN	NaN	NaN	62.50	0.0080	0.0021
PLCKG264.4+19.5	264.42	19.48	6.15	null	NaN	NaN	NaN	NaN	32.25	0.0028	0.0010
PLCKG115.7+17.5	115.72	17.53	6.78	null	NaN	NaN	NaN	NaN	17.48	0.0025	0.0008